Geophysical Journal International

Geophys. J. Int. (2022) **231,** 749–769
Advance Access publication 2022 June 14
GJI Geomagnetism, Rock Magnetism and Palaeomagnetism

https://doi.org/10.1093/gji/ggac213

Rock magnetic fingerprint of Mt Etna volcanic ash

Luigi Vigliotti [1], Dario Bilardello,[2] Aldo Winkler[3] and Paola Del Carlo[4]

[1] *Istituto di Scienze Marine, ISMAR-CNR, Via P. Gobetti* 101, 40129 *Bologna, Italy, luigi.vigliotti@bo.ismar.cnr.it*
[2] *Institute for Rock Magnetism, University of Minnesota, Minneapolis, MN 55455, USA*
[3] *Istituto Nazionale di Geofisica e Vulcanologia, Sezione di Roma2, Via di Vigna Murata* 605*, 00143 Rome, Italy*
[4] *Istituto Nazionale di Geofisica e Vulcanologia, Sezione di Pisa, Via Battisti* 53*,* 56125 *Pisa, Italy*

Accepted 2022 June 9. Received 2021 November 10; in original form 2022 May 31

SUMMARY

A detailed rock magnetic study was conducted on ash samples collected from different products erupted during explosive activity of Mount Etna, Italy, in order to test the use of magnetic properties as discriminating factors among them, and their explosive character in particular. Samples include tephra emplaced during the last 18 ka: the benmoreitic Plinian eruptions of the Pleistocene Ellittico activity from marine core ET97-70 (Ionian Sea) and the basaltic Holocene FG eruption (122 BC), the Strombolian/Phreatomagmatic/sub-Plinian eruptions (namely, the Holocene TV, FS, FL, ETP products and the 1990, 1998 eruptions) collected from the slope of the volcano, and the Recent explosive activity (lava fountains referred to as '*Ash Rich Jets and Plumes*', or ARJP) that occurred in the 2001–2002 period, related to flank eruptions. Mössbauer spectrometry informs that a single magnetic mineral dominates the three groups, which are characterized by variable magnetic grain sizes and composition. Detailed rock-magnetic investigations, ranging from low temperature to high temperature remanence and susceptibility experiments, indicate that the more explosive products of the Plinian eruptions and ARJP activity tephra, are characterized by oxidized Ti-rich titanomagnetites, with dominant Curie Temperatures between 230 and 330 °C. The FG and ARJP tephra are also characterized by contrasting, yet overall higher, coercivity distributions and higher magnetizations and susceptibilities, including below room temperature. In contrast, most of the Strombolian/sub-Plinian eruptions have a magnetic signature dominated by less coercive magnetite and/or Ti-poor titanomagnetite. Magnetic differences observed between the Late Pleistocene and Holocene FG Plinian eruptions can be attributed to the different composition of the former eruptions, which were fed by more evolved magmas, whereas geochemical variations characterizing the products erupted in the last few decades can be responsible for the differences between the Holocene and recent Strombolian/sub-Plinian products. Importantly, detailed magnetic investigation of sideromelane and tachylite clasts, the two end members of the juvenile fraction extracted from the ash of the most explosive products, determines that the tachylite fraction is responsible for the magnetic signature of the Plinian FG and ARJP tephra, and is attributed to the intense fragmentation that characterizes these activities, likely resulting from undercooling processes. Moreover, the abundant superparamagnetic grains associated with these eruptive styles are believed to represent the nanolite fraction responsible for the increasing viscosity of these magmas, and to be responsible for their explosive character. The distinctive magnetic properties that characterize the tachylite-bearing tephra, representative of the fragmentation process that distinguishes the most explosive activities, provides a useful magnetic tool that can complement traditional volcanological investigations.

Key words: Magnetic properties; Europe; Rock and mineral magnetism; Explosive volcanism; Volcaniclastic deposits.

1 INTRODUCTION

One of the biggest challenges in volcanology is to understand the mechanism of explosive eruptions, identify the resulting deposits and finally reconstruct the volcanic processes leading to different volcanic activities. A volcano may exhibit both effusive (lava effusion) and explosive activity (e.g. Strombolian, sub-Plinian, Plinian) during different eruptions or even within the same event, complicating the understanding of the underlying mechanisms. Geochemical techniques provide information on magma composition, but these analyses cannot always distinguish deposits from different volcanic events (Smith *et al*. 2011). Such information might be critical for both reconstructions of eruption history and the identification of individual volcanic layers.

Mount Etna, located on the eastern coast of Sicily (Italy; Fig. 1), is the largest and most active volcano in Europe. It is considered a volcano-laboratory for its persistent activity characterized by eruptions of effusive nature and explosive activity. The latter activities range from Strombolian to sub-Plinian events that only rarely evolve into Plinian, such as the 122 BC eruption that formed the 'Il Piano' caldera (Fig. 1; Coltelli *et al.* 1998). Explosive activity produced lapilli and ash fallouts up to hundreds of kilometres from the source (Branca & Del Carlo 2005). Since 1986, Etna has shown an extraordinarily high number of explosive events, with more than 240 episodes (Del Carlo *et al.* 2004; Andronico *et al.* 2021, and references therein), better known as paroxysms, from summit craters. In 2001 and 2002, two flank eruptions occurred, characterized by long-lasting explosive activity at several vents along the eruptive fissures. This prolonged activity produced lava fountaining and Strombolian events, and was responsible for the ejection of a great amount of volcanic ash into the atmosphere and widespread (thousands of km) fallout deposits (Andronico *et al.* 2005, 2008, 2009; Scollo *et al.* 2007). In particular, concerning the 2002 flank eruption, on the basis of textural, compositional and morphological investigations of erupted ash, Andronico *et al.* (2009) indicate that the dominant style of explosive activity consisted of distinct magma jets with transition to other eruptive styles, including Strombolian and ash explosions. Similarly, ash-rich explosive activity was also observed during the 2001 flank eruption of Etna (Taddeucci *et al.* 2002; Andronico *et al.* 2009), and was interpreted as transitional between different styles of basaltic explosive activity (Andronico *et al.* 2009). The authors suggested the term '*ash-rich jets and plumes*' (ARPJ) to describe lava fountains producing cooler, finely fragmented magma in the form of tachylite-rich ash. These lava fountains are significantly different from classic Hawaiian-type lava fountains that generate hotter magma clots that are ejected as fine glassy particles (siderome-lane; Head & Wilson 1989). According to Andronico *et al.* (2009), Etna Hawaiian fountains and ARJP erupt tephra with contrasting morphology and componentry: sideromelane dominates the first, whereas tachylite characterizes the latter. Eruptive conditions leading to the formation of tachylite and sideromelane are not well understood, although differences in the chemical and morphological features have been related to different cooling processes (Heiken & Wohletz 1985).

How and why the eruptive style changes within the same volcano is discussed by Dingwell (1996): 'flow or blow?'. Brittle magma fragmentation is responsible for highly explosive activity especially in basaltic magma. For silicic magmas this type of fragmentation is attributed to high strain rates associated with acceleration of the bubbly mixture (Dingwell 1996; Gonnermann & Manga 2003; Gonnermann 2015) or to bubble overpressure (Kueppers *et al.*). Conversely, these conditions are difficult to achieve for basaltic

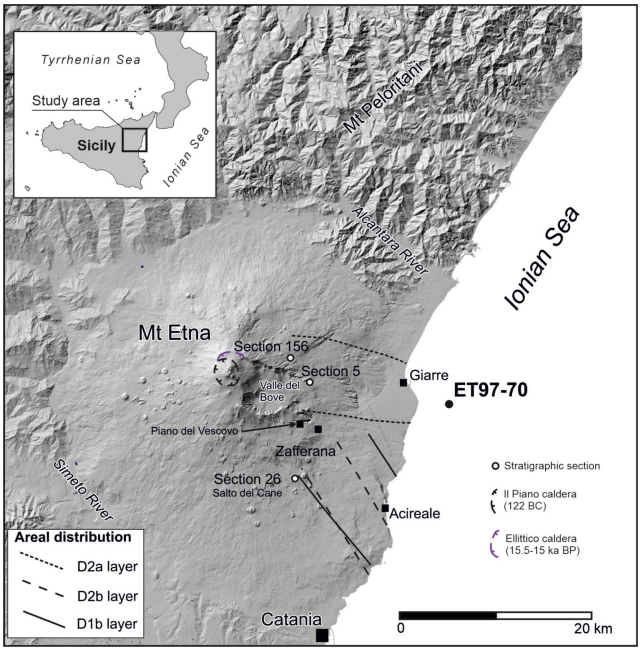

Figure 1: Map of the Etna region with the location of the studied samples.

magma which is characterized by low viscosity (Giordano & Dingwell 2003), so the processes responsible for the fragmentation of this type of magma are still debated (Cassidy *et al.* 2018). A viscosity increase driving the fragmentation can be obtained by crystallization during magma ascent in the volcanic conduit (Cashman & Blundy 2000; La Spina *et al.* 2015). Another process can be magma ascent rates dependence on the high decompression rate of magma, which is a function of the pressure within the magma reservoir, the location of the fragmentation surface, the viscosity, and the geometry of the conduit (Sparks *et al.* 1999). Recent experiments have challenged the timing of the crystallization process demonstrating the key role played by undercooling processes in basaltic Plinian eruptions, such as the 122 BC event (Arzilli *et al.* 2019).

Iron oxides are almost ubiquitous in volcanic materials. A handful of studies have used palaeomagnetic data to identify eruptive activity and to correlate tephra deposits (e.g. Knott *et al.* 2020; Risica *et al*. 2020; Westgate *et al.* 2018; William-Jones *et al*. 2020). However, only few results have shown the potential of magnetic techniques to characterize tephra layers (Maenaka & Yokoyama 1972; Lagroix *et al.* 2004; Till *et al.* 2011; Makaroglu *et al.* 2018; Naumov *et al.* 2019) or pyroclastic flow deposits (Bowles *et al.* 2013; Jackson & Bowles 2014; Vigliotti 2015), and to our knowledge, their relationships with the eruptive styles have been investigated only for the Paintbrush tuff in Nevada (Rosenbaum 1986; Schlinger *et al.* 1988, 1991), the tephra layers of the Mitina Maar in the Czech Republic (Lied *et al.* 2020), and the deep sea 2012 Havre rhyolite eruption (Knafelc *et al*. 2022).

The magnetic signature of the fragmentation affecting the most explosive eruptions is likely expressed as magnetic grain size, which in turn can be affected by the cooling rate, low temperature oxidation and exsolution due to the breakdown of the solid solution between ulvospinel (Fe_2TiO_4) and magnetite (Fe_3O_4). Explosive eruptions are usually controlled by temperature, composition and crystallization of the magma (e.g. Dingwell 1996). Experimental data by Di Genova *et al.* (2020), corroborated by other observations, indicate that presence of nanolites can trigger volcanic explosions, but these might be difficult to identify in explosive

products. For (titano)magnetite-bearing rocks, magnetic hysteresis parameters (e.g. Day *et al.* 1977) provide the most rapid means to characterize the particles' domain states to a first-order approximation (e.g. Roberts *et al.* 2018). Definitive information about these characteristics, however, can only be obtained in conjunction with other magnetic methods (FORC diagrams; low temperature experiments), particularly when dealing with variations in magnetic grain size within the same specimen, variations in stoichiometry, stress state, oxidation and other parameters (Roberts *et al.* 2019).

Aim of this study is to identify the magnetic signature of the different eruptive styles of explosive events occurring at Etna. We pay particular attention to the content of the tachylite and sideromelane end members of the juvenile fraction, whose relative content varies depending on the eruptive type.

2 MATERIALS

Tephrostratigraphic studies have reconstructed the explosive activity of Etna for the last 100 ka and identified five tephra-layer units (A–E), produced by eruption styles ranging from Strombolian to Plinian (Coltelli *et al.* 2000). In this work we have studied tephra belonging to the units D (Late Pleistocene) and E (Holocene), that is the past 18 ka. Moreover, we have also analysed some ash samples erupted during summit and flank eruptions in the last decades.

In particular, Unit D consists of Plinian benmoreitic-trachytic pumice deposits, called D1a-D2a and D1b-D2b (Coltelli *et al.* 2000) and formerly known as the Biancavilla Ignimbrite eruptions (De Rita *et al*. 1991). These eruptions are responsible for the emplacement of widespread tephra layers recorded in marine and lacustrine records of the Mediterranean region and labelled differently depending on the locality (Y1, Et-1, TM-11, TM-12; Albert *et al*. 2013, and references therein). The duration of the entire cycle of eruptions and the correlations with distal counterparts in the Mediterranean area are still under debate (Albert *et al.* 2013; Del Carlo *et al.* 2017).

Products of Holocene unit E are produced by sub-Plinian to Strombolian eruptions and one Plinian event, the 122 BC eruption (FG tephra; Coltelli *et al*. 1998). Finally, we analysed ash samples produced by summit and flank explosive eruptions characterized by shifts from Strombolian to ARJP activity (Andronico *et al*. 2008; 2009), occurred in the period 1990–2002, which we call Recent.

Specifically, and separated by eruptive style, we analysed (Table 1):

2.1 Plinian eruptions (Late Pleistocene unit D and 122 BC from Holocene Unit E)

Twenty-eight samples (cubic plastic boxes of 2 × 2 × 2 cm) of ash representing the complete Unit D (thickness 56 cm) were sampled from the bottom of the ET97-70 marine core recovered in the offshore of Catania (Fig. 1). On the basis of magnetic susceptibility profiles we correlated the bottom of the core and the interval between the two groups of eruptions (D1a-D2a and D1b-D2b) to calibrated ^{14}C ages (18.586–18.859 ka BP and 17.249–17.901 ka BP, respectively) carried out on a core (ET99-M11) collected from the Alfeo Seamount in the Ionian Sea (Vigliotti *et al.* 2011). The age at the bottom of the core overlaps with the onset of the unit D activity (18.533–18.818 ka BP) reported by Coltelli *et al.* (2000). The age of the interval separating the two groups of eruption is in good agreement with the age of the base of the D2a unit (18.019–18.560 ka BP), as well as with the age of the final D2b eruption (16.965–17.670 ka BP, Albert *et al.* 2013), supporting our correlation. The timing between the different eruptions suggests that at least the interval between the two groups of eruptions include marine sediment mixed with tephra, therefore, most of the interpretations for this interval are based on the ash sample occurring at 80-81 cm of the core section, which represents an instantaneous event from the D2a eruption (ET97-70/80-81), void of marine sediment contamination. We also focus on the sample ET97-70/54-56 representative of the D2b eruption. Additionally, the sampling was supplemented by an ash sample from core PALB94-1E/851.5 retrieved from Albano Lake (∼500 km distance to the North) and correlated with the Y1 unit by Calanchi *et al.* (1996). Although, as suggested by Albert *et al.* (2013) for a similar tephra found in the nearby Mezzano Lake, it could be equivalent to a younger tephra from the Monticchio Lake record (TM-11).

Two samples from Unit E were collected at the Monte Salto del Cane outcrop (section 26; Fig. 1). These samples belong to the basal ash of the 122 BC Plinian eruption (unit A of Coltelli *et al.* 1998).

2.2 Strombolian/sub-Plinian eruptions (Holocene Unit E and recent activity)

Nine ash samples from the Strombolian-sub-Plinian eruptions of the Unit E including seven samples from late Holocene eruptions and two samples from recent activity. The former includes few marker beds identified by Del Carlo *et al.* (2004): TV (one sample from section 26 and one sample from section 156); FS (one sample from section 5); FL (two samples from section 26); and a Strombolian eruption (two samples), here labelled ETP, collected from an outcrop on the volcano flank (Fig. 1). In particular, FS is an olivine-rich pyroclastic fall deposit produced by a sub-Plinian eruption (3930 ± 60 BP) representing a rare example of picritic magma erupted on Etna (Coltelli *et al*. 2005), TV is a varicoloured tuff layer (5340 ± 60 BP) and FL samples are from tuff layers corresponding to the phreatoplinian phase of the eruption (3150 ± 60 BP; Coltelli *et al.* 2000). The ETP samples correspond to a Strombolian deposit related to the emplacement of a dike at Section 26 (Fig. 1) and dated at 2100 BP ± 200 by Tanguy *et al.* (2012).

The recent activity is represented by two samples belonging to the sub-Plinian eruptions that occurred in 1998 (22-07-1998) and 1990 (Bronte 1990), produced by paroxysmal episodes from the summit craters (Scollo *et al.* 2013).

2.3 Explosive Ash-Rich Jets and Plumes eruptions (2001-2002 flank eruptions)

The collection includes one sample from the initial hydromagmatic phase of the 2001 eruption, two samples representing the whole 2002 eruption collected on the volcano flank at Piano del Vescovo (ET02-PV) and near Zafferana (ET02-Zf; Fig. 1), and six samples representing daily events. The latter six ash samples represent key intervals (initial stage: 30th October–1st November; bulk of the first cycle: 9–10th November; final stage: 1st and 8th December) of the evolution of the eruption from October to December 2002 (Andronico *et al.* 2005). We refer to these recent samples as ARJP sensu Andronico *et al.* (2008, 2009).

To better discriminate the magnetic properties of fragmentation, the two end members of the juvenile ash, tachylite (microlite-rich clasts) and sideromelane (glassy clasts), ejected during the 2002 flank eruption and 122 BC Plinian eruption, were separated under

Table 1: List of the studied samples from the three groups of tephra, listing sampling location, ages (L. Pl. and L. Hol correspond to Late Pleistocene and Late Holocene, respectively, for recent samples the date of the eruption is reported), eruptive style (ARJP represents *ash-rich jets and plumes*), composition, and selected magnetic properties: hysteresis parameters (M_{rs}/M_s, B_c, B_{cr} and the sigma shape-parameter (Fabian 2003); Curie temperatures determined from the warming curves of the thermomagnetic experiments; LT data: %χ (20–300 K), per cent of the difference between χ at 20 and 300 K; %M-RTSIRM (C–W) the per cent of magnetization after cooling/warming experiments between 10 and 300 K; χ'-Peak (K) the temperature showing the largest frequency dependence of χ; K (χ-Max Fd%), the temperature over which the χ' peak occurs at 1 Hz of frequency (χ'peak); C-1 Unmix (mT), the coercivity of the dominant component distributions unmixed from the backfield curves.

Age	STYLE	Composition	Mr/Ms	Bc [mT]	Bcr [mT]	SIGMA	Curie T(°C)	%χ (20–300 K)	%M-RTSIRM (C-W)	χ'-Peak (K)	K (χ-Max Fd%)	C-1 Unmix (mT)
Late Pleist.	Plinian	Benmoreite	0.22	19.9	49.6	–0.0337						
Late Pleist. (2b)	Plinian	Benmoreite	0.21	18.6	46.7	–0.0338						
Late Pleist.	Plinian	Benmoreite					245/569					
Late Pleist.	Plinian	Benmoreite	0.15	12.9	40.7	–0.0105						
Late Pleist. (1b)	Plinian	Benmoreite	0.18	13.5	41	–0.0144						
Late Pleist.	Plinian	Benmoreite	0.18	14.4	39.6	–0.0436						
Late Pleist. (2a)	Plinian	Benmoreite	0.12	11.2	39.6	–0.0035	232/561	37	16.8	65	50	49
Late Pleist.	Plinian	Benmoreite	0.21	16.9	42.4	–0.0789						
Late Pleist. (1a)	Plinian	Benmoreite	0.18	14.3	44.5	–0.0121						
Late Pleist.	Plinian	Benmoreite	0.15	12	37.7	0.0114						
Late Pleist.	Plinian		0.19	14		0.0253						
			Mr/Ms±St-Dev	**Bc[mT]±St-dev**	**Bcr±St dev**		**Curie T(°C)**	**%χ (20-300K)**	**%M-RTSIRM (C-W)**	**χ'-Peak (K)**	**K (χ-Max Fd%)**	**C-1 Unmix (mT)**
Late Pleist.	**Plinian**		**0.18±0.03**	**14.8±2.8**	**424±3.8**		**238±9-565±6**	**37**	**16.8**	**65**	**50**	49
L. Hol - 122BC	Plinian	Hawaiite	0.21	19	47.9	0.0036	256					73.4
L. Hol. - 122BC	Plinian	Hawaiite	0.21	17.2	45.4		310	23-24	5.3	65	70	
			Mr/Ms±St-Dev	**Bc[mT]±St-dev**	**Bcr-mean±St dev**		**Curie T(°C)±StD**	**%χ (20-300K)**	**%M-RTSIRM (C-W)**	**χ'-Peak (K)**	**K (χ-Max Fd%)**	**C-1 Unmix (mT)**
L. Hol	**Plinian**		**0.21**	**18.1**	**46.7**		**283±19**	**23.5**	**5.3**	**65**	**70**	**73.4**
L. Hol. - 5340 BP	Sub-Plinian-/Phreatom.	Hawaiite	0.19	17.7	39.9	–0.0985						
L. Hol. - 5340 BP	Sub-Plinian-/Phreatom.	Hawaiite	0.20	18.5	41.5	–0.0873	512	45	14.6	45	45	44.7
L. Hol. - 3930 BP	Sub-Plinian	Picritic-Basalt	0,24	19.8	41.7	-0.11						
L. Hol. - 3150 BP	Stromb-/Phreatom.	Mugearite	0.18	15.7	34.4	–0.0708						36.4
L. Hol. - 3150 BP	Stromb-/Phreatom.	Mugearite	0.20			–0.0813	257/553	35-36	15.1	45	50	
L. Hol. - 150 BC	Strombolian						565					
L. Hol. - 150 BC	Strombolian		0.19	15	34.3	–0.0316	270/565					
1990	Sub-P/Phreat.	Basalt	0.07	3.4	16.8	–0,1388	320					
1998	Sub-Plinian	Basalt	0.09	6.1	36.8	0.0525						60
			Mr/Ms±St-Dev	**Bc[mT]±St-dev**	**Bcr-mean±St dev**		**Curie T(°C)±StD**	**%χ (20-300K)**	**%M-RTSIRM (C-W)**	**χ'-Peak (K)**	**K (χ-Max Fd%)**	**C-1 Unmix (mT)**
L. Hol.	**Stromb./sub-Plinian**		**0.17±0.06**	**13.8±6.4**	**35±8.6**		**282±34-549±25**	**40.3±4.7**	**15.05**	**45**	**47.5**	**47±12**
			0.106/0.048	**6.92/3.95**	**31/12.4**							
2001	Phreatom./ARJP	Basalt	0.16	11.2	39.5	0.0606						
2002	ARJP	Hawaiite	0.11	9.71	48.4	0.0836	330	19-20	7.0	65	70	114.8
2002	ARJP	Hawaiite	0.09	6.57	40.8	0.1090	335					
2002	ARJP	Hawaiite	0.18	14.4	55.8	0.0564	355					
2002	ARJP	Hawaiite	0.15	11.5	62.6	0.1378	355					
2002	ARJP	Hawaiite	0.19	15.3	73.1	0.1098	365	22	4.6	60	70	
2002	ARJP	Hawaiite	0.14	11.5	23.5	–0.0006	372					
2002	ARJP	Hawaiite	0.20	13.5	64.2	0.1714						
2002	ARJP	Hawaiite	0.20	20.1	67.4	0.0349	291/539					100
			Mr/Ms±St-Dev	**Bc[mT]±St-dev**	**Bcr-mean±St dev**		**Curie T(°C)/StD**	**%χ (20-300K)**	**%M-RTSIRM (C-W)**	**χ'-Peak (K)**	**K (χ-Max Fd%)**	**C-1 Unmix (mT)**
2001-2002	**ARJP**		**0.16±0.04**	**12.6±3.8**	**52.8±16**		**343±27**	**20.8±1.3**	**5.5±1.2**	**62.5**	**70**	**107.4**
L. Hol.	Plinian	Sideromelane	0.10	6.5	25.8	–0.025						38.9
2002	ARJP	Sideromelane	0.10	6.36	26.5	0.062		20	9.7	60		33.1
			Mr/Ms±St-Dev	**Bc[mT]±St-dev**	**Bcr-mean±St dev**			**%χ (20-300K)**	**%M-RTSIRM (C-W)**	**χ'-Peak (K)**	**K (χ-Max Fd%)**	**C-1 Unmix (mT)**
L. Hol-Recent	**P-ARJP**		**0.1±0.01**	**6.43±0.07**	**26.2+/-0.4**			**20**	**9.7**	**60**	**70**	**36±2.9**
L. Hol.	Plinian	Tachylite	0.26	23.3	60	0.0020						74.9
2002	ARJP	Tachylite	0.19	16.7	72.7	0.0844		20-21	4.2	65		108.2
			Mr/Ms±St-Dev	**Bc[mT]±St-dev**	**Bcr-mean±St dev**			**%χ (20-300K)**	**%M-RTSIRM (C-W)**	**χ'-Peak (K)**	**K (χ-Max Fd%)**	**C-1 Unmix (mT)**
L- Hol-Recent	**P-ARJP**	**Tachylite**	**0.23±0.05**	**20±3.3**	**66.4±6.4**			**20**	**4.2**	**65**	**70**	**91.6±16.6**

the microscope. It is important to mention that while both components were isolated from the same highly explosive products, sideromelane is more typical of Strombolian activity (e.g. Cannata *et al.* 2014).

3 METHODS

Selected samples were first analysed with a stereo microscope for textural and component analyses at the laboratories of the Istituto Nazionale di Geofisica e Vulcanologia, Sezione di Pisa. A full set of rock magnetic experiments were carried out to determine the magnetic mineralogy and the magnetic grain size at the Institute for Rock Magnetism at the University of Minnesota, following preliminary magnetic measurements (magnetic susceptibility, anhysteretic and isothermal remanence experiments) performed at the Palaeomagnetism Laboratory at ISMAR-CNR Bologna, and high-temperature analyses carried out at the Palaeomagnetic Laboratory of the CNRS at Gif-sur-Yvette (France). For some samples, hysteresis properties were double-checked at the Palaeomagnetic Laboratory of INGV, Rome. We acquired First-Order Reversal Curves (FORCs), hysteresis loops and backfield DC demagnetization remanence curves (DCD or Backfield curves) at room temperature on Princeton Measurements Corporation (Princeton, NJ) Vibrating Sample Magnetometers (VSMs). FORC data were processed using the FORCinel software package (Harrison & Feinberg 2008) in conjunction with the VARIFORC smoothing protocol of Egli (2013). Coercivity spectra were derived from the absolute values of the backfield hysteresis curves for selected samples and their unmixing was performed using the MAX UnMix software (Maxbauer *et al.* 2016).

Low temperature (LT) experiments were conducted on Quantum Design (San Diego, CA) Magnetic Properties Measurement Systems (MPMS-XL and 5S). LT experiments were carried out by measuring the magnetic remanence on warming from 10 K to room temperature (300 K) after cooling in a 2.5 T field (field cooled remanence, FC), as well as after cooling in zero field and applying a saturation isothermal remanent magnetization (SIRM) of 2.5 T at 10 K (zero-field cooled remanence, ZFC). A room temperature (RT) 2.5 T SIRM was also applied at 300 K and the remanence was measured upon temperature cycling to 10 K and back (RTSIRM). AC susceptibility as a function of temperature and frequency (1, 10 and 100 Hz or 1, 5, 32, 178 and 1000 Hz) was also measured for selected specimens from the three groups of samples.

Room temperature susceptibility measurements as a function of field amplitude (10, 20, 40, 80, 120, 200 and 400 A m^{-1}) were carried out on the Late Pleistocene samples using a Magnon susceptibility system. Saturation magnetization on warming between room temperature and 700 °C (M_s–T) was measured on selected specimens using a horizontal Curie balance with Argon gas circulation to limit oxidation processes during heating. Likewise, magnetic susceptibility on warming between room temperature and 700 °C (χ–T) was measured on a Kappabridge KLY-2 (Brno, Czech Republic) using fields of 300 A/m and 920 Hz. M_s–T and χ–T curves are collectively referred to as thermomagnetic curves. Three samples (ET97-70/80-81, S26-TV and 1/11/2002), were investigated by Mössbauer spectroscopy at room (295 K) and low (18–20 K) temperature.

Two samples from the TV tephra and tachylite clasts from the FG tephra were analysed by means of elements chemical mapping and point analyses using an Environmental Scanning Electron Microscope (ESEM) Zeiss EVO LS 10, equipped with an Energy-Dispersive Spectroscopy (EDS) device Bruker Quantax system, Esprit software at the Institute of Microelectronics and Microsystem (IMM) of CNR at Bologna.

4 RESULTS

4.1 Magnetic susceptibility

The susceptibility profile for the 28 ash samples collected from Core ET97-70 exhibits a magnetic signature characterized by four major peaks that correlate with the two couples of Plinian eruptions: D1a (ET97-70/90-92)-D2a (ET97/70-80-81 cm) and D1b (ET97-70/64-66 cm)-D2b (ET97-70/52-56 cm, Fig. 2) of stratigraphic Unit D. The highest peak (ET97-70/80-81) occurs for the D2a eruption, consisting in loose ash visibly characterized by overall larger grain size. Field-dependent susceptibility is higher for most of the samples of the initial eruptions D1a-D2a, with respect to the upper ashes (Fig. 2). A contribution of marine sediments is certainly responsible for the minimum susceptibility values occurring on the top and between 67 and 77 cm of depth that represent the interval dividing the two main eruptions.

4.2 Hysteresis parameters and FORC diagrams

Hysteresis (Fig. 3) clearly defines two different behaviours among the studied tephra. The most significant difference is given by the presence of wasp-waisted hysteresis loops (positive sigma values (Fabian, 2003) for the Plinian FG and Recent ARJP eruptions, indicating the presence of magnetic components with contrasting coercivity (Tauxe *et al.* 1996), whereas the remainder of the Strombolian/sub-Plinian and a few Plinian eruption have more parallel to pot-bellied (negative sigma) hysteresis loops (Fig. 3 and Table 1).

The FORC diagrams for most samples have coercivity distributions (B_c) limited to below 0.15 T, whereas those of the FG and the Recent tephra extend to above 0.2 T, indicating the contribution of a harder magnetic fraction in these samples (Fig. 4). An exception is for the FS tephra sample corresponding to the rare picritic magma eruption, which, although sub-Plinian, also has a coercivity distribution extending above 0.2 T. All FORC diagrams have increased vertical spread at low values of B_c defining a somewhat triangular shape distribution, diagnostic of vortex to multidomain (MD) grains (e.g. Egli, 2021), some tephra possessing a clear indentation along a 135° diagonal (e.g. ET-97-70-I 64-66 and 80-81, PALB94-1E/851.5, SVP 293-TV, ETP-2, S26-FL), diagnostic of the vortex state (e.g. Egli 2021).

On a Day *et al.* (1977) plot (Fig. 5a), hysteresis parameters [saturation remanent magnetization (M_{rs})—saturation magnetization (M_s) ratio versus the coercivity of remanence (B_{cr})—coercivity (B_c) ratio] for all samples plot in the central 'pseudo-single domain' (PSD) region, with distributions that are mostly parallel to the theoretical mixing trends for single domain (SD)–(MD) magnetite particles of Dunlop (2002), yet shifted upwards. Provided the ambiguities and limits of the Day plot (e.g. Roberts *et al.* 2018, 2019), we also present hysteresis parameters on a Néel diagram or squareness plot (M_{rs}/M_s versus B_c, Tauxe *et al.* 2002), where the lines provide the theoretical prediction of a mixing of uniaxial single domain and superparamagnetic (SP) grains with axial ratios of 1.3:1 and 2:1 (Fig. 5b). On such diagram the spread of data along these lines, as for the strombolian/sub-Plinian data (in blue), for example,

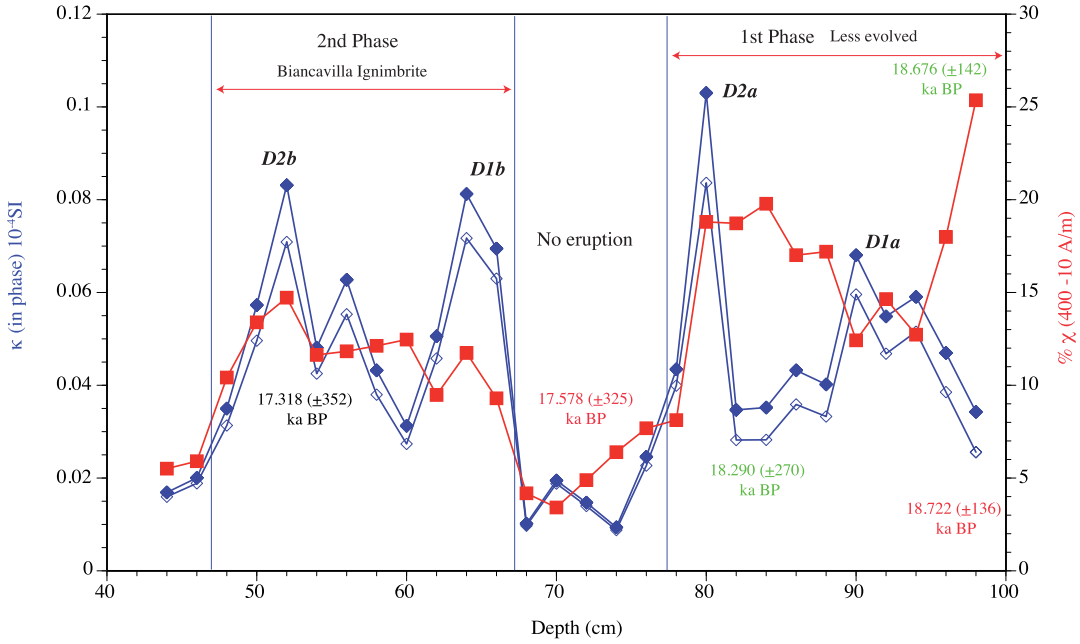

Figure 2: Magnetic susceptibility data of samples from Core ET97-70 (Late Pleistocene tephra). Blue symbols refer to in-phase susceptibility at different alternating field amplitudes: 10 A m^{-1} (open symbols) and 400 A m^{-1} (solid symbols). Red squares refer to the percentage of amplitude-dependence of the susceptibility between the two applied fields. The ages reported in the plot represent datings of the eruptions published by different authors: Albert *et al.* (2013) (black colour), Coltelli *et al.* 2000 (Green colour), Vigliotti *et al.* 2011 (red colour); see text for details.

which appeared clustered on the Day plot, is somewhat increased, although to some extent it is a matter of scale. In both diagrams, the difference between the sub-Plinian 1990 and 1998 eruptions, compared to the strombolian eruptions, is striking. Moreover, and particularly on the Néel plot, the former data show pronounced similarities with the sideromelane fraction extracted from the most explosive (Plinian and ARJP) eruptions, as opposed to the tachylite fraction from the same eruptions which tends to plot at the opposite end of the distribution (Fig. 5b). Scatter is still present, however, and the sub-Plinian picritic FS sample, for example, also plots at the extreme end of the diagram close to the data for the tachylite extracts.

4.3 Thermomagnetic curves

Most of the strombolian/sub-Plinian tephra (TV, FL and ETP), are characterized by magnetite or Ti-poor titanomagnetite, showing Curie temperatures (T_C) in their χ–T curves of ~510–565 °C suggesting minor Ti-substitution for this class of samples (Table 1). Samples lose all susceptibility by 580 °C and show some production/loss of magnetite during the experiment (TV/FL, Fig. 6). Specimen S26b-FL also has an inflection at ~260 °C on both warming and cooling curves, and although the higher-temperature inflection is suppressed on cooling, the absolute values of susceptibility <200 °C remain constant.

χ–T curves for the Pleistocene Plinian tephra (ET97-70) have inflection points at ~230–245 °C, corresponding to the T_C of Ti-rich titanomagnetite, and a second inflection at ~560–570 °C, corresponding to magnetite's T_C, beyond which the samples are completely demagnetized (Fig. 6). The sample representing the Unit D2a (ET97-70-80/81) indicates an initial loss of susceptibility when cooling down to ~250 °C and the susceptibility below this temperature is equivalent on both the heating and cooling curves (Fig. 6). On the contrary, the sample from the upper D2b eruption (ET97-70/54-56, *cf*. Fig. 6) shows an increase of susceptibility during cooling below ~570 °C, indicating production of secondary magnetic minerals (likely low Ti titanomagnetite) on warming.

The Plinian FG tephra, instead has a first loss of susceptibility on warming at ~260 °C, and a secondly, somewhat smaller inflection ~475 °C, with all susceptibility lost above ~550 °C. In the cooling curve, the higher temperature inflection is no longer present, and the low temperature inflection is reproduced and increases somewhat in susceptibility (Fig. 6).

χ–T curve of the ARJP eruptions are characterized by a significant inflection at temperatures below 300 °C, indicating that titanium-rich titanomagnetite dominates the magnetic response of these samples. The curves are roughly reversible, with a minor increase in the susceptibility on cooling (Fig. 6), whereas full reversibility is observed during a second heating/cooling cycle (Fig. S3).

Summarizing, χ–T curves indicate the dominant presence of T_C <300 °C in the Plinian and ARJP samples, whereas dominant higher T_C (>540°) where identified in the Holocene Strombolian/sub-Plinian samples.

M_s–T curves overall bear similarities to the χ–T curves (Fig. S3). One exception, for which we do not have a susceptibility curve, is that of the sub-Plinian tephra from the Bronte 1990 eruption, which bears striking similarities with the most explosive Plinian and ARJP samples, with a dominant T_C of 320 °C, before losing all its magnetization >500 °C.

4.4 Low temperature measurements

Low temperature experiments clearly show differences between the studied samples. Both in-phase (χ) and out of phase susceptibilities (χ') increase from 10 to 300 K in the Plinian FG and ARJP samples (Figs 7a–c), whereas smaller increases with increasing temperature

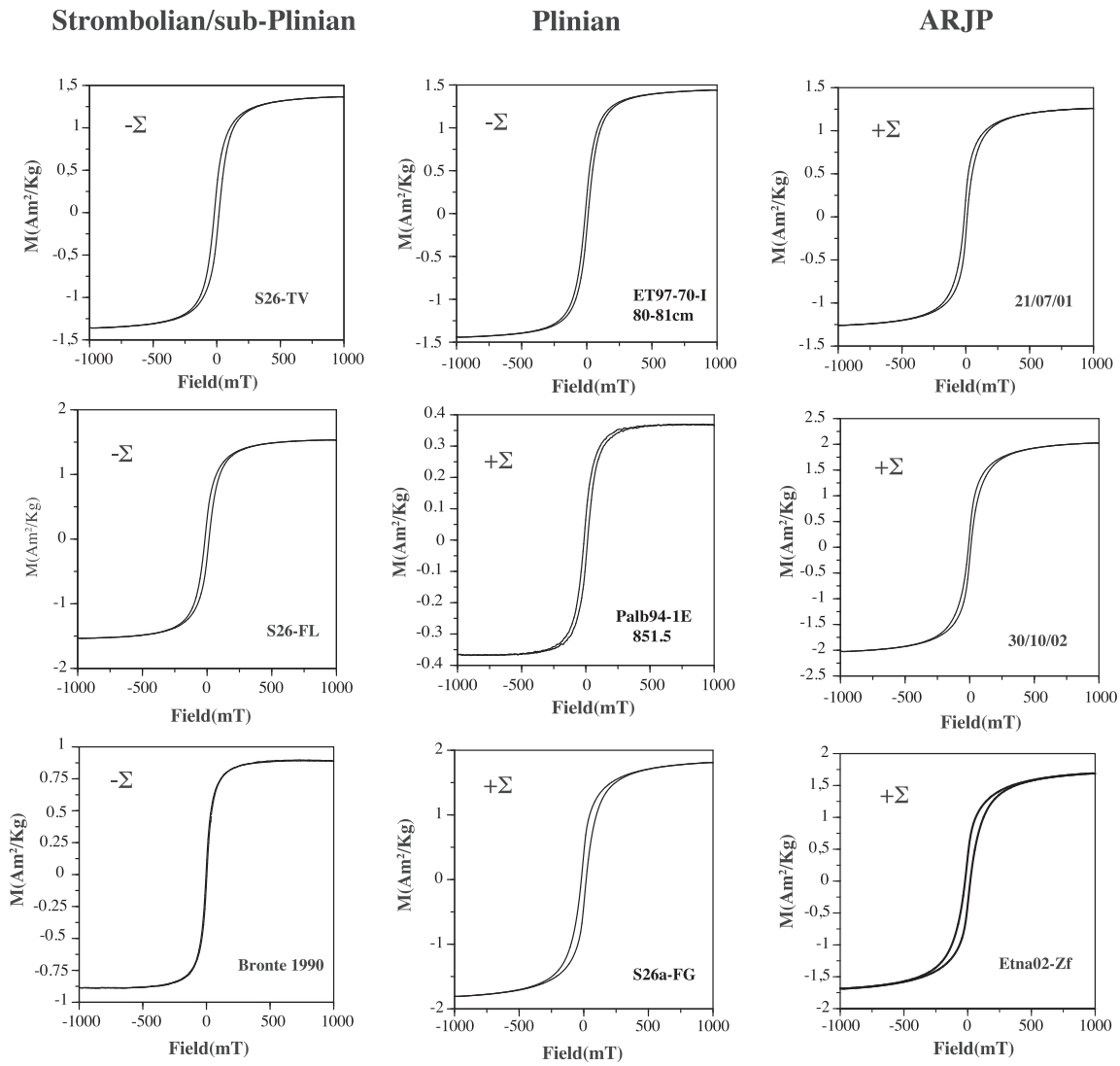

Figure 3: Hysteresis loops for selected tephra samples arranged by eruptive style. Relevant hysteresis parameters are reported in Table 1, note the dominant wasp-waisted character of the Recent ARJP and Late Holocene FG tephra. The symbol Σ denotes the sigma-shape parameter of Fabian (2003) where positive (negative) values correspond to wasp-waisted (pot-bellied) loops (see text for details).

are observed in the samples from the Pleistocene Plinian D2a, as well as for sub-Plinian FL and TV samples (Figs 7d–f). Furthermore, the absolute values of both χ and χ' differ remarkably between the two groups, with higher susceptibility for the FG and recent ashes.

Frequency dependence is most prominent between ∼40 and 110 K for χ of all samples whereas χ' data are more sensitive to frequency, with differences among samples: the Recent ARJP samples, together with the Plinian D2a and FG sample, show a well defined χ' peak at 60–65 K that shifts to higher temperatures (100–105 K) and larger magnitude with increasing frequency (Figs 7a–d). This peak occurs at somewhat lower temperatures (45–80 K) for the sub-Plinian FL and TV samples (Figs 7e–f; Table 1). A second χ' peak, also with a significant frequency dependence, occurs around 270 K for the Plinian FG and Recent ARJP ashes, and is not as well defined for the Plinian D2a, and sub-Plinian FL and TV samples.

FC and ZFC remanence curves for all specimens decrease from low to room temperature, with the FC remanence somewhat stronger than the ZFC and decreasing more rapidly up to ∼50 K, after which both curves have similar intensities and decrease gently until room temperature (Figs 8a–e for the derivatives of these curves and Fig. S4 for the unprocessed data). These curves are typical for titanomagnetite (e.g. Moskowitz *et al.* 1998) containing a mixture of SD and MD grains (Carter-Stiglitz *et al.* 2006; Kosterov & Fabian, 2008; Kasama *et al.* 2013). Clear evidence of the Verwey transition (T_V) is only visible in the derivative of both the FC and ZFC curves of the Late Pleistocene Plinian ET97-70/80-81 sample and the sub-Plinian TV and FL tephra (Figs 8a–c).

RTSIRM data indicate that the magnetization increases on cooling down to about 130–140 K (ARJP and Plinian FG tephra), after which the magnetization remains fairly constant to 10 K, or ∼200 K (Plinian ET97-70/80-81, sub-Plinian TV and FL tephra), before decreasing somewhat to ∼50 K. Warming curves have similar trends and define a similar 'hump' as the cooling curves for these samples. Most of the magnetization of the Plinian FG and ARJP samples is recovered, with only a small amount (5.3 and 7 per cent, respectively) of the total room temperature remanence lost (Fig. 8f and Table 1), however, the amount of magnetization lost at room temperature is higher for the Plinian ET97-70/80-81, and sub-Plinian TV and FL tephra (∼17 and ∼15 per cent, respectively).

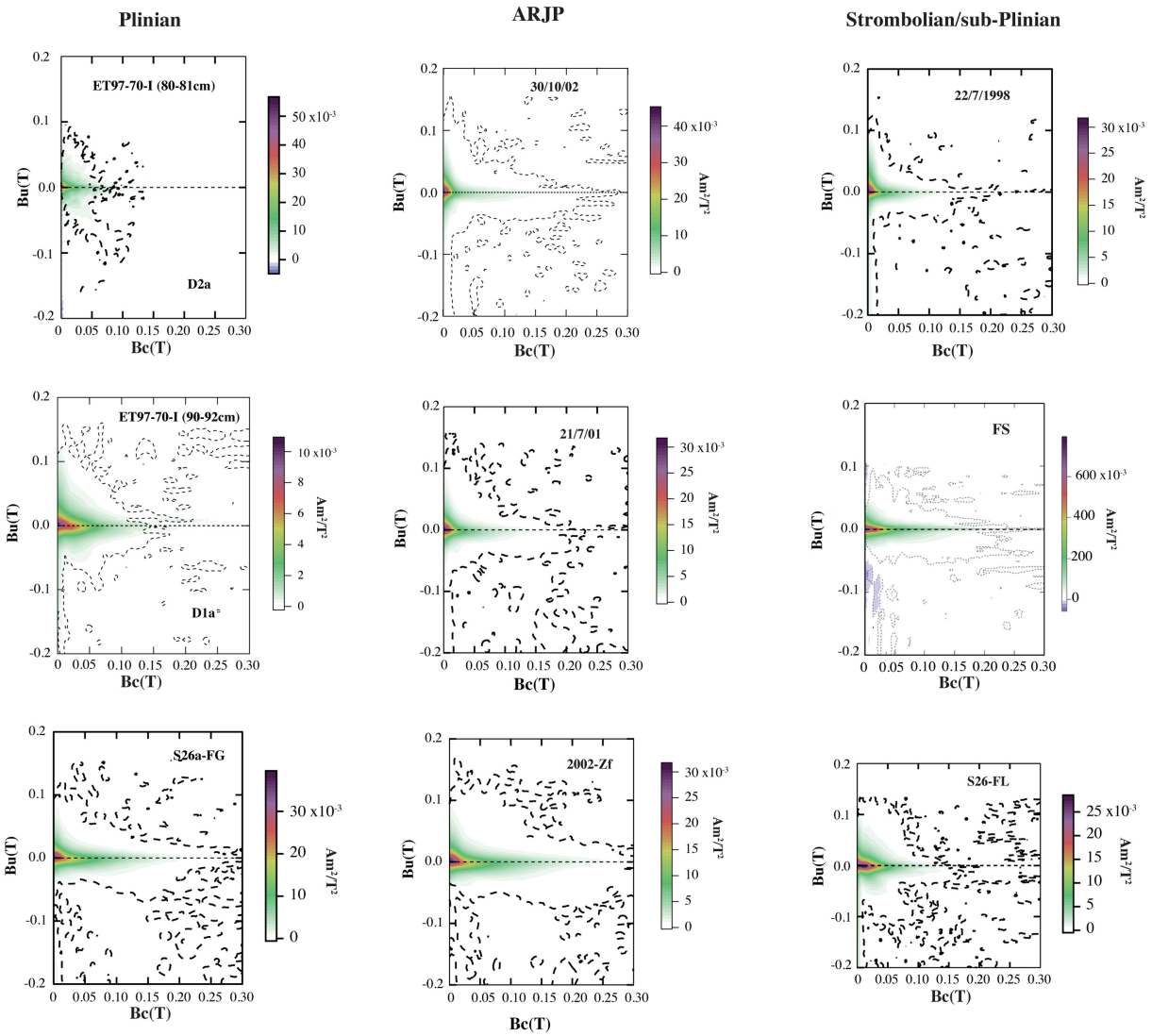

Figure 4: FORC diagrams for selected tephra samples for the three eruptive style classes. For direct comparison, samples are plotted using the same horizontal and vertical scale (see text for details). Note the higher coercivity distribution characterizing the most explosive Plinian (FG) and ARJP tephra (see text for details).

4.5 Coercivity distribution

Unmixing modelling of backfield curves indicate that remanence is held by two or three magnetic components. The coercivity spectra of the Plinian ET97-70/80-81, and Strombolian/sub-Plinian TV and FL tephra can be fitted with two components represented by a dominant distribution accounting for ∼86–89 per cent of the total remanence, and B_{cr} values comprised between ∼36 mT (1.56 $\log_{10}B$) and ∼49 mT (1.69 $\log_{10}B$, Fig. 9). The secondary component has lower coercivity, between 3.6 mT for the Plinian tephra (ET97-70/80-81) and 5-11 mT for the Holocene strombolian/sub-Plinian TV and FL samples (Fig. 9). Recent ARJP and Plinian FG tephra show a primary high coercivity component centred between ∼60 mT (1.78 $\log_{10}$ B) and ∼115 mT (2.06 $\log_{10}B$) for the Recent ARJP ash, and ∼75 mT (1.87 $\log_{10}B$) for the Plinian FG tephra. This component represents ∼62 per cent of the magnetization of the FG tephra and ∼43–60 per centof that of the recent samples. An intermediate component is characterized by a coercivity of ∼17–27 mT representing ∼23–51 per centof the magnetization of the Plinian FG and Recent ARJP, while a minor component 3 (∼6–9 per cent for the ARJP and ∼16 per cent for the FG tephra), is fitted at very low coercivity values (∼1.8–3.5 mT). Three components are also identified in the Recent Strombolian/sub-Plinian sample 22/07/98 that shows a coercivity distribution (C1: ∼60 mT) similar to the ARJP and to the FG tephra, yet somewhat still lower (Fig. 9).

4.6 Tachylite-sideromelane magnetic signature

Magnetic properties of the tachylite (microlite-rich fragments) and sideromelane (glassy fragments) clasts separated from the 2002 ARJP and Plinian FG tephra point out to significant differences between these two juvenile-ash endmember components (Fig. 10). Hysteresis data show that the tachylite has magnetization values, M_s and especially M_{rs}, about two to five times larger than the sideromelane (Fig. 10 and Table 1). However, the most significant differences occur in the coercivity, as shown by differences of one order of magnitude in the hard isothermal remanent magnetization (HIRM), and B_{cr} values increasing from ∼26 mT in the sideromelane to ∼66 mT in the tachylite (Table 1). This difference is well identified

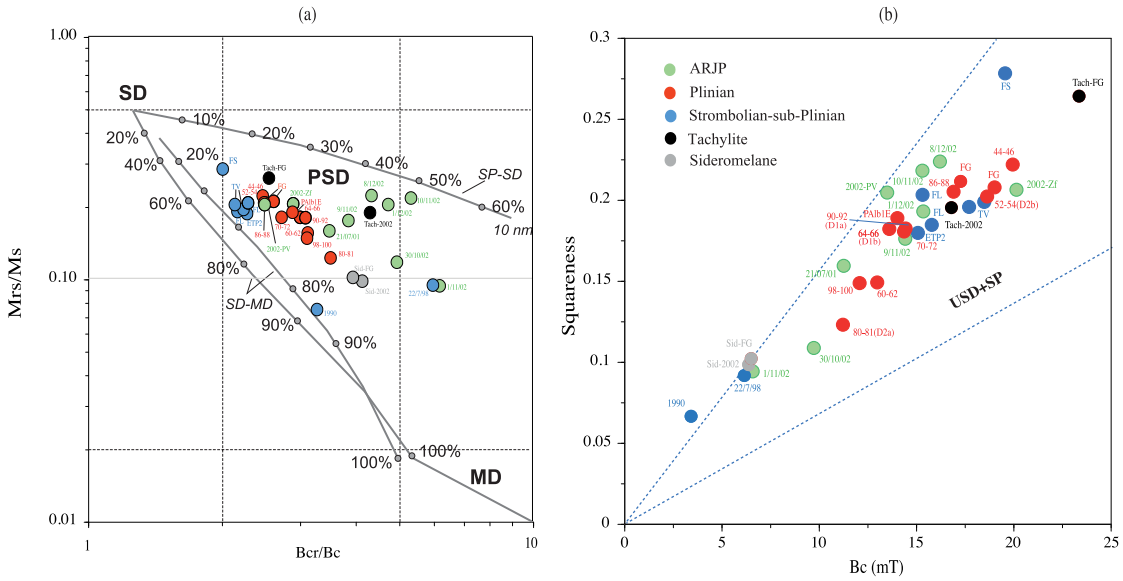

Figure 5: Modified Day plot (a) and Néel plot (b) of the studied samples. The solid lines in the Day plot are the theoretical mixing lines for SD + MD grains and SD + SP grains of Dunlop (2002). The area between the dashed lines in the Néel plot refers to the theoretical prediction of squareness and coercive field of uniaxial single domain (USD) + superparamagnetic (SP) grains with axial ratios of 1.3:1 and 2:1 (Tauxe *et al.* 2002).

by the unmixing models, with the tachylite showing three components dominated by a distribution centred ∼75–108 mT (1.87–2.03 $\log_{10}B$, Fig. 10). An intermediate component 2 (∼25–30 mt) represents ∼21 per cent of the magnetization of the tachilite from the Plinian FG sample and ∼38 per cent of the younger sample (ARJP ash). An additional minor (∼2–4 per cent lower coercivity component is present in the tachylite samples. On the other hand, the sideromelane is dominated (84–92 per cent by a component with a coercivity peak comprised between ∼33 and 39 mT (1.52 and 1.59 $\log_{10}B$), whereas lower coercivities contributing to the remanence are fit with one broad low-intensity component (Fig. 10). Moreover, the tachylite presents strongly wasp-waisted hysteresis loops as opposed to the narrow loops of the sideromelane fraction (Fig. 9 and Table 1), and FORC distributions characterized by a ridge extending past 0.2 T along the B_c axis, while FORC distributions for the sideromelane do not exceed 0.12 T along B_c (Fig. 10).

Low-temperature measurements exhibit minor differences between the two components, however, the tachylite systematically retains higher magnetizations and susceptibilities compared to the sideromelane. In particular, χ' curves possess two distinct peaks for either fraction, centred at ∼60–100 K (frequency increases with temperature) and ∼260–280 K, with the per cent of frequency dependence reaching >7–9 per cent at around 70 K for the sideromelane, and somewhat smaller dependence, ∼6–6.5 per cent, for the tachylite at the same temperature, although the measurement frequencies used are not identical among the two specimens (Fig. 10). RTSIRM magnetization curves indicate an increase on cooling until ∼120–130 K, with a subsequent slight decrease, and remains constant to 10 K. On warming, the sideromelane shows a larger loss of the SIRM remanence at room temperature (9.7 per cent) compared to the tachylite (4.2 per cent). No magnetite Verwey transition (∼120 K) is observed, including in the derivatives of the FC and ZFC curves, which instead show sharp drops in magnetization on warming at ∼50 and 60 K for the sideromelane and tachylite fractions, respectively (Fig. 10).

4.7 Mössbauer spectroscopy

Mössbauer spectra were recorded for samples ET97-70/80-81 (Plinian), 1/11/2002 (ARJP) and S26-TV (Strombolian) at 18–20 K and also at 295 K for the first two samples (Fig. S1), using a 25-mCi ^{57}Co source in a Rh matrix and a constant acceleration drive and transmission geometry. The positions of the absorption lines for each iron site are diagnostic of different iron oxides and the fitted parameters are reported in Table S1. For sample ET97-70/80-81, at 295 K the sextet corresponding to the Fe^{3+} tetrahedral site A is characterized by a hyperfine field (B_hf) of 49.16 T and isomer shifts of 0.31 mm s^{-1} whereas for the mixed valence '$Fe^{2.5+}$' octahedral site B the hyperfine field and isomer shift are 46.63 T and 0.47 mm s^{-1}. At 20 K, these positions are 52.46 and 51.29 T, and 0.49 and 0.4 mm s^{-1}, respectively. The spectra for sample S26-TV at 20 K is characterized by a hyperfine field (B_hf) of 52.31 T and isomer shifts of 0.46 mm s^{-1} for the tetrahedral site A, whereas for the octahedral site B the hyperfine field and isomer shift are 50.67 T and 0.46 mm s^{-1}. For sample 1/11/2002, at 295 K the tetrahedral site A is characterized by a hyperfine field (B_hf) of 45.1 T and isomer shifts of 0.26 mm s^{-1} whereas for the octahedral site B the hyperfine field and isomer shift are 44.15 T and 0.51 mm s^{-1}. At 18 K, these positions are 51.43 and 50.81 T, and 0.53 and 0.4 mm s^{-1}, respectively.

5 DISCUSSION

The magnetic properties of Mt Etna tephra indicate the presence of titanomagnetite as the main remanence carrier, with variable titanium substitution, and magnetic grain size mixture. Key magnetic parameters useful to discriminate among samples belonging to different eruptive styles (Plinian, Strombolian/sub-Plinian, ARJP) are reported in Table 1.

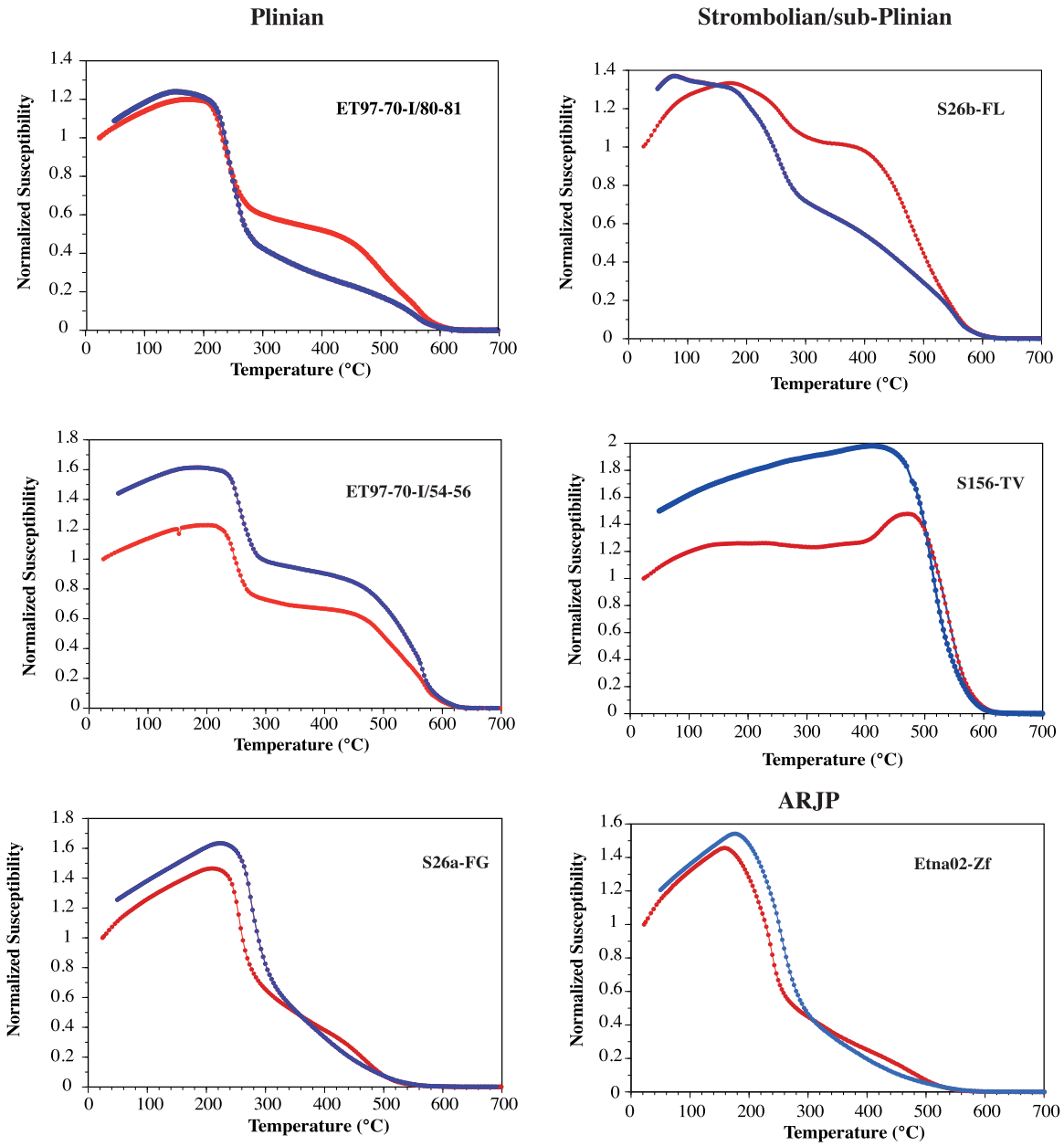

Figure 6: χ–T experiments for selected samples of Etna tephra grouped by explosive character: Plinian (ET97-70 I/80-81 and 54–56, FG S26b), Strombolian/sub-Plinian (S26bFL and TV) and ARJP (Etna02-Zf). Red (blue) colour refers to heating (cooling) curves (see text for details).

5.1 Magnetic mineralogy and stoichiometry

The fitted Mössbauer Spectra parameters (Table S1) are consistent with those of magnetite, which, in its pure form, at room temperature contains two sextets corresponding to the tetrahedral A-site (hyperfine field B_{HF} 49.2 T and isomer shift 0.26 mm s^{-1}) and octahedral B-site (B_{HF} 46.1 T and isomer shift 0.67 mm s^{-1}). At 4.2 K, pure magnetite sextets for both sites have parameters B_{HF} 52.5 T and isomer shift 0.48 mm s^{-1} for A, and B_{HF} 50.1 T and isomer shift 0.45 mm s^{-1}, for B. Titanium substitution necessarily changes the distribution of Fe cations in the tetrahedral and/or octahedral sites (e.g. Bowles *et al.* 2013, and references therein) and particularly broadens the peaks of the B sites. In maghemite spectra, sites A and B are less distinct, with hyperfine fields B_{HF} of 50.0 and 52 T and isomer shifts of 0.35 and 0.48 mm s^{-1} at room temperature and 4.2 K, respectively. No hematite-like sextet fits are present at either temperature, suggesting that no antiferromagnetic phase is present in our samples, and the spectra can be interpreted with reasonable confidence as titanium substituted magnetite-maghemite.

The χ–T (and M_s–T, Fig. S2) curves for the Plinian and ARJP eruptions, show pronounced Curie temperatures ∼230–330 °C and a second Curie temperature ∼550–580 °C (Fig. 6), the former suggesting pronounced titanium substitution in the lattice (e.g. Dunlop & Ozdemir 1997; Jackson & Bowles 2014). In addition, the warming curve of the Plinian FG tephra also shows a pronounced loss of susceptibility ∼475 °C, which can be interpreted as susceptibility carried by a finer grain size fraction. χ–T curves below room temperature for these samples, except ET97-70/80-81, show that susceptibility increases pronouncedly between 15 and 300 K displaying significant frequency dependence (Figs 7a–c), in agreement with Ti substitution (Moskowitz *et al.* 1998). On

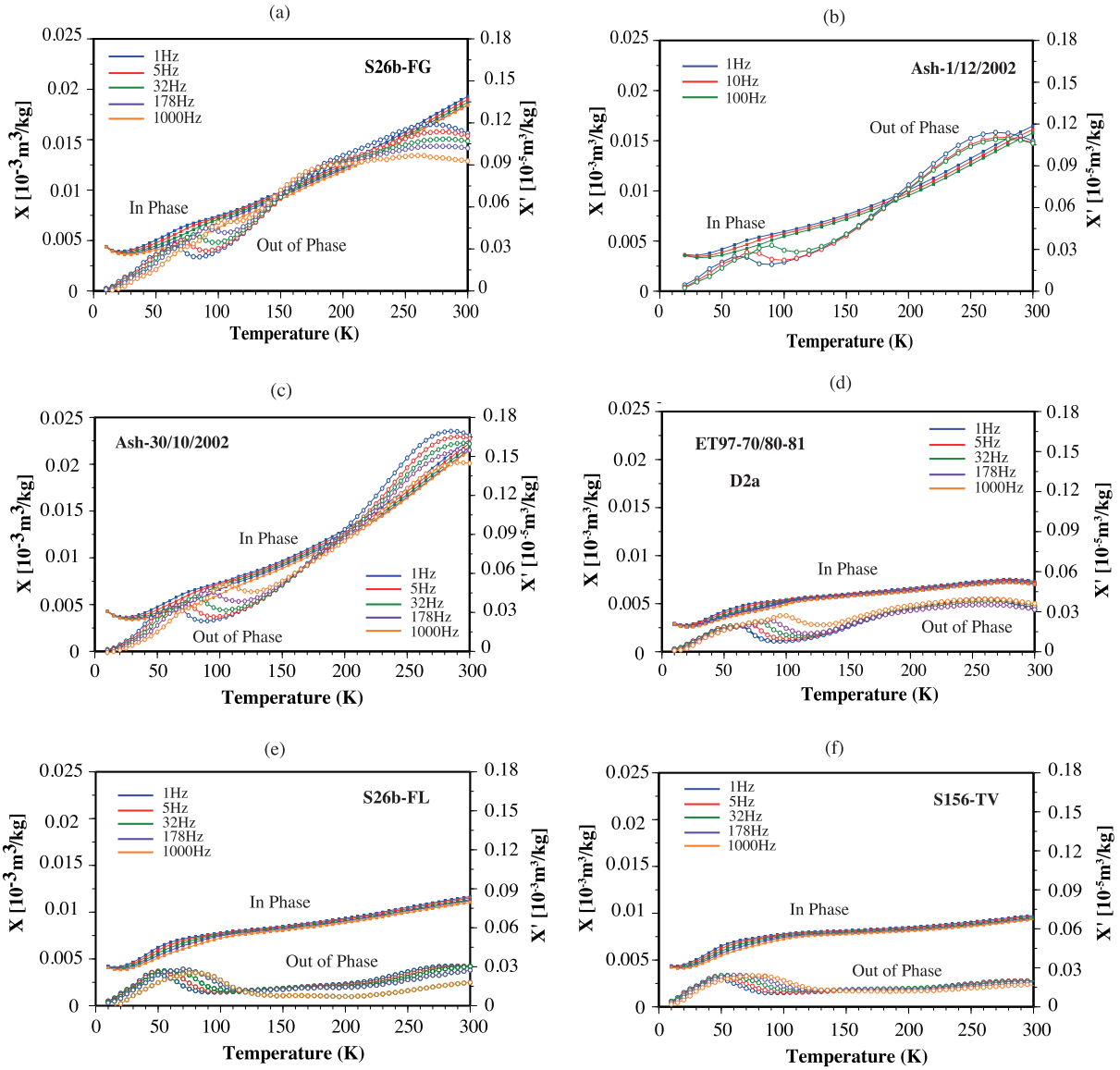

Figure 7: In-phase (close symbols), χ, and out-of-phase (open symbols), χ' frequency-dependent susceptibility between 10 and 300 K for selected tephra samples belonging to the three eruptive groups: (a–b) Plinian; (c–d) ARJP; (e–f) Strombolian-sub-Plinian. Three or five different frequencies were used between 1 and 1000 Hz, as specified in the figure. For direct comparison, samples are plotted using the same scale (see text for details).

the contrary, the Strombolian/sub-Plinian eruptions TV, FL and ETP have χ–T curves dominated by Curie temperatures in the 550–580 °C range, but specimens FL and ETP also possess a smaller inflection at ∼275 °C (Fig. 6 and Table 1). Unlike specimen TV, for which the cooling curve has larger susceptibility than the heating curve, indicative of alteration and production of magnetite on heating, specimens FL and ETP have lower susceptibility on cooling, indicating suppression of the more stoichiometric magnetite fraction, but the susceptibility below ∼200–275 °C remains approximately the same, indicating reversibility of the bulk measurement.

At low temperature, specimens TV and FL possess a more gradual increase of susceptibility towards room temperature, also exhibiting less frequency dependence, consistently with more stoichiometric magnetite (Figs 7e–f). In other titanium-bearing pyroclastic samples, Bowles *et al.* (2013) and Jackson & Bowles (2014) had observed phases with distinct Curie temperatures in the 325–475 °C and 540–580 °C ranges, which were determined to correspond to different proportions of homogeneous titanomagnetites and oxyexsolved grains with ilmenite lamellae within magnetite, respectively. Because ilmenite is paramagnetic above room temperature, the higher Curie temperatures were interpreted to correspond to the more stoichiometric magnetite fraction of the oxyexsolved grains. According to those authors, the proportions of the homogeneous and oxyexsolved grains are controlled by the emplacement temperatures and cooling history of the rocks and do not reflect magma compositional variations, where the higher Curie temperatures are observed primarily in samples that had cooled from above 600 °C, allowing for the grains to oxyexsolve. Jackson & Bowles (2014) report low temperature in-phase susceptibility data for some thermally-annealed specimens, which were shown to produce oxyexsolution upon annealing. These curves are characterized by strong increases in warming, like those reported here. However, they clearly identify a sharp drop below ∼273 K, indicating the presence of a phase

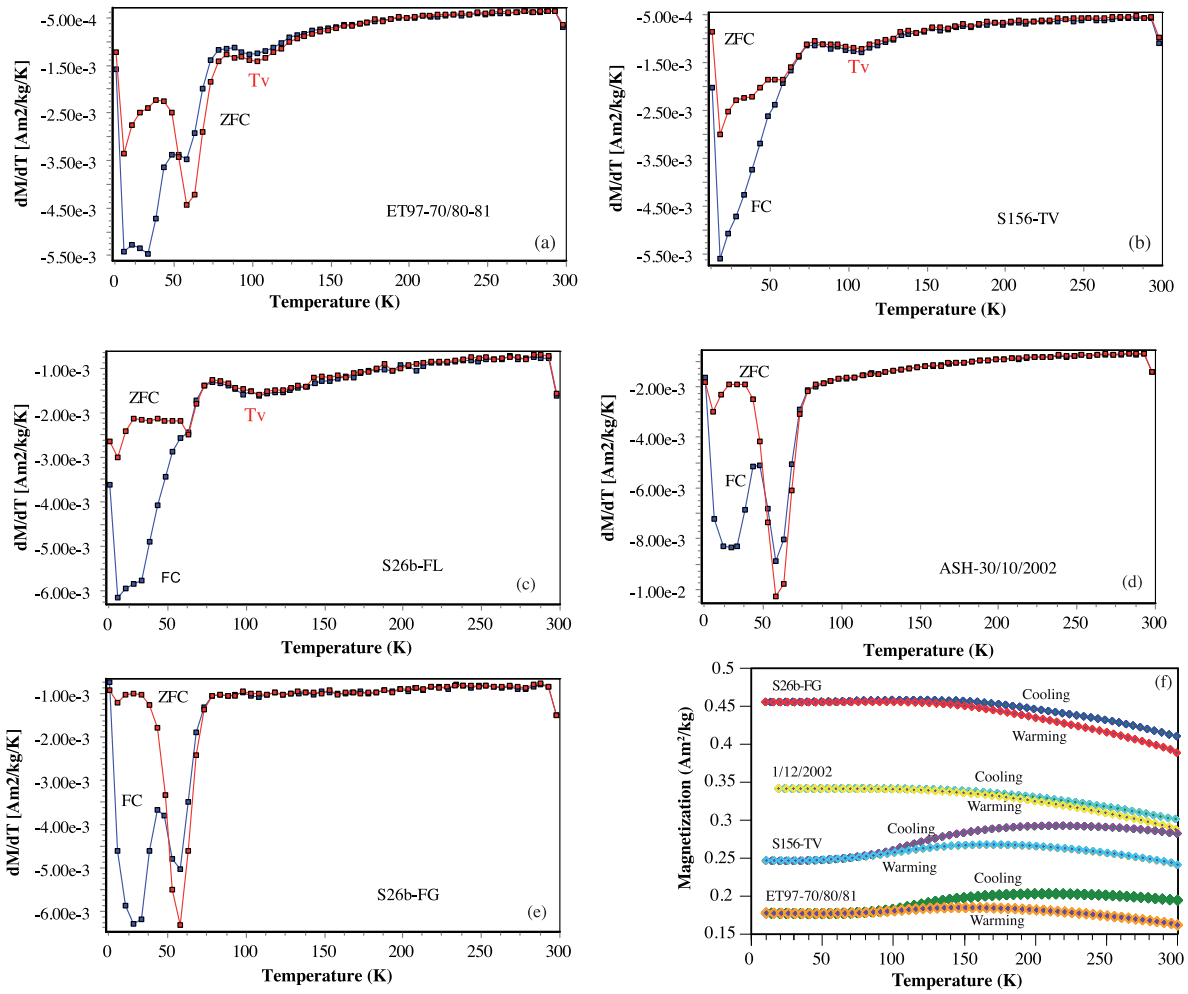

Figure 8: Direct current (dc) magnetic remanence experiments for selected different-aged tephra samples belonging to the three eruptive groups, carried out by measuring the magnetic remanence on warming from 10 K to room temperature (300 K) after cooling in a 2.5 T saturation isothermal remanent magnetization (SIRM, field cooled remanence, FC, blue), as well as after cooling in zero field (ZFC, red) and applying a low temperature 2.5 T SIRM. Results are expressed as the first derivatives for two Plinian samples (a–b), a Recent ARJP ash (c), two Strombolian/sub-Plinian samples (d–e). T_V marks the position of the magnetite Verwey transition which occurs in the Plinian ET97-70/80-81 and in the Strombolian/sub-Plinian TV and FL tephra. Panel (f) shows the results of selected samples from the same groups after applying a room temperature SIRM (RTSIRM experiment) and measuring the remanence upon cooling and warming to the same temperatures as the experiments above.

containing 75–80 paer cent mole fraction of ilmenite. Unfortunately, they do not report low temperature susceptibility data for unannealed samples, precluding a direct comparison to our data. χ–T curves above room temperature for the same treated samples possessed two Curie temperatures at 540 and 580 °C, indicating a Ti-poor titanomagnetite (20–40 per cent titanium substitution) and a nearly stoichiometric magnetite.

Similarly, in other tephra, Lagroix *et al.* (2004) also identify a titanium-rich phase of the ilmenite–hematite series, by frequency-independent peaks/drops at 210 K (χ) and at 190 K (χ'), corresponding to a change in magnetic ordering to paramagnetism above these temperatures, and were thus interpreted as Curie or Néel temperatures attributed to titanohematite with ∼80 per cent titanium substitution. Moreover, they conclude that high titanium phases of the ilmenite–hematite series, magnetically disordering to paramagnetism below room temperature, can be quickly and effectively recognized, even in low concentration, by the LT frequency-dependent in phase and out of phase susceptibilities.

A comparison of our data and those of Lagroix *et al.* (2004) and Jackson & Bowles (2014) suggests that for the Plinian eruptions of the Late Pleistocene and Holocene FG, and ARJP Recent tephra, the more prominent 230–255 °C T_C corresponds to homogeneous titanomagnetite with ∼50–60 per cent titanium substitution and the less pronounced ∼550–580 °C T_C corresponds to more stoichiometric magnetite. Alternatively, the lower T_C could in fact correspond to a 40–50 per cent- titanium substituted hematite oxyexsolved from a precursor titanomagnetite, whereas the higher temperature T_C phase represents the more stoichiometric magnetite fraction of those oxyexsolved grains. The latter would imply magma emplacement temperatures >600 °C with no homogeneous titanomagnetite preservation in these samples.

On the other hand, the Strombolian/sub-Plinian TV, FL and ETP tephra, which are instead dominated by 540–570 °C T_C on heating, prevalently contain more stoichiometric magnetite, which, following Jackson and Bowles (2014) is, if not primary, the result of oxyexsolution. In this case, the oxyexsolved titanohematite, for which an obvious T_C in the χ–T curves is not visible, must be paramagnetic

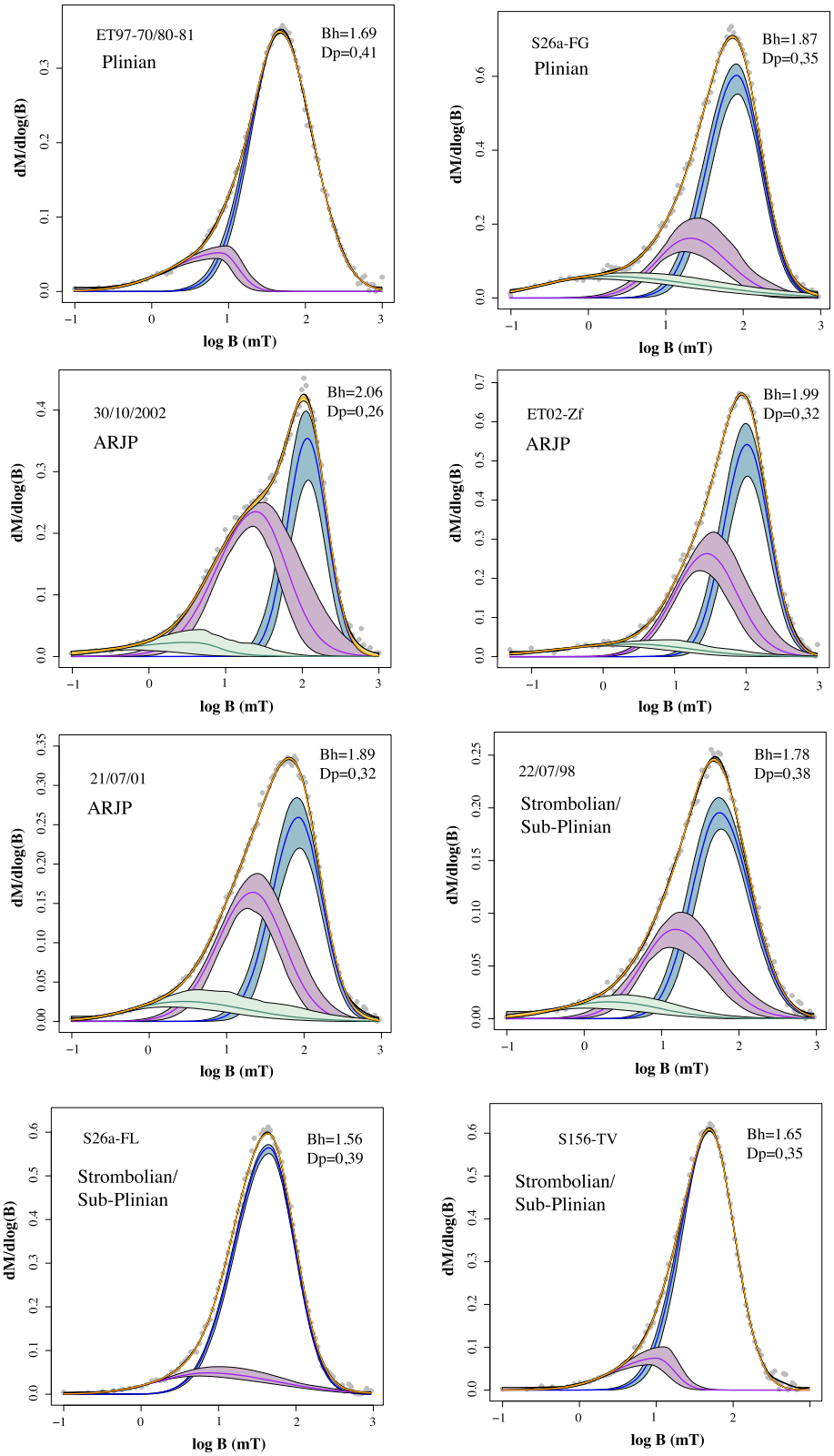

Figure 9: Unmixing of backfield curve remanence data for different samples of the three groups of tephra (Plinian, Strombolian/sub-Plinian, ARJP) obtained by using the MAX UnMix software (Maxbauer *et al*. 2016). See text for details.

>RT and no appreciable homogeneous titanomagnetite is present. However, no obvious features that would indicate titanohematite are observed in LT susceptibility (Fig. 7). Jackson and Bowles (2014) demonstrated that the oxyexsolution obtained upon experimentally annealing their samples can be undone by cooling from temperatures above $\sim$ 500 °C, as in a χ–T experiment, 'regenerating' a titanomagnetite T_C (*cf*. their fig. 8 where a T_C of 388 °C is produced on cooling from 600 °C). This does not occur in our samples, and

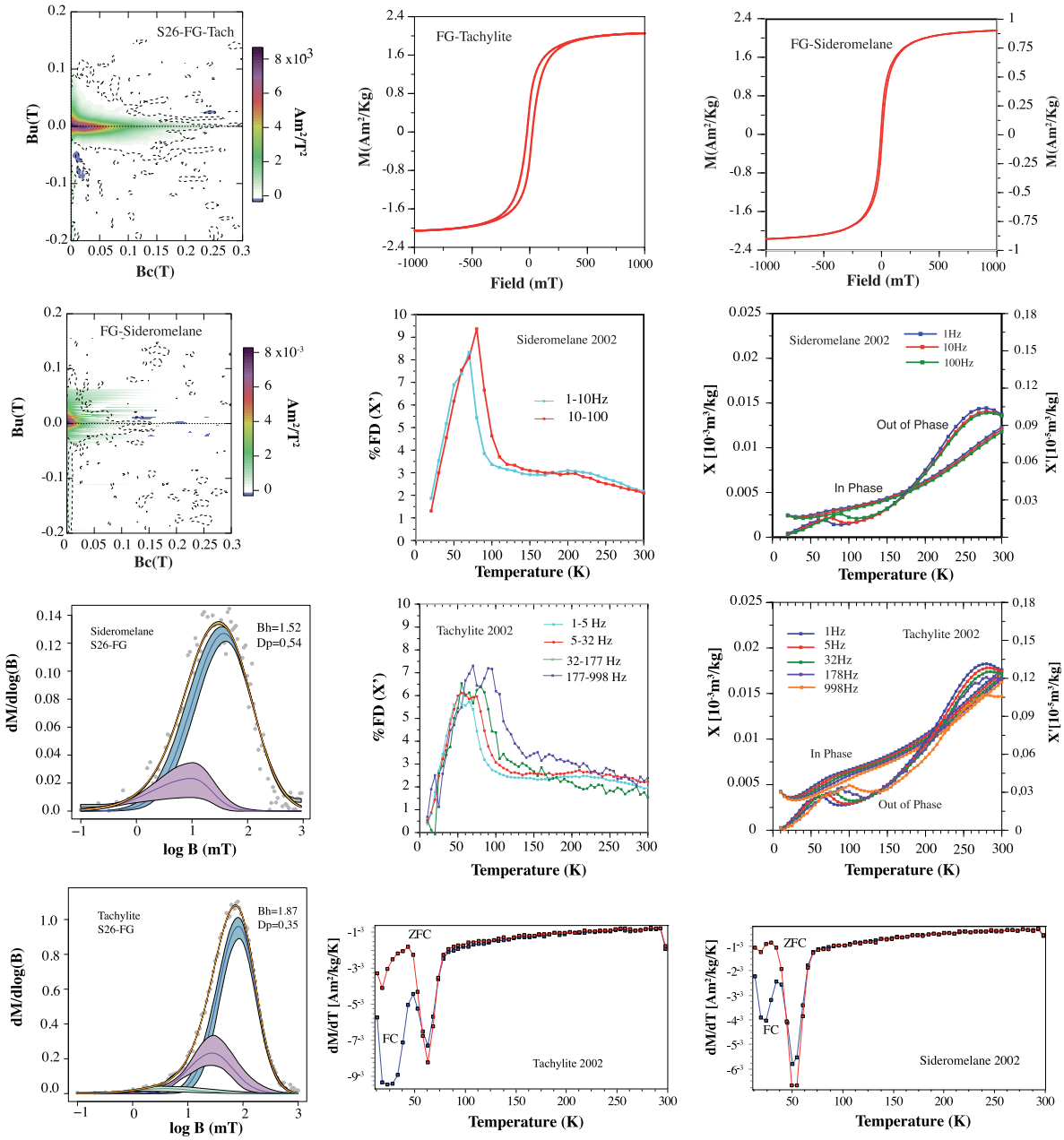

Figure 10: FORC diagrams, hysteresis loops, low temperature (LT) experiments and backfield remanence unmixing modelling for tachylite and sideromelane extracts collected from the Plinian FG and 2002 ARJP tephra samples. LT data include FC and ZFC (first-derivatives shown); in-phase, χ, and out-of-phase, χ' frequency-dependent susceptibility experiments; per cent of frequency dependence of χ' between 1 and 100 Hz for the sideromelane and 1–998 Hz for the tachylite (see text for details).

particularly in the TV tephra which only shows the stoichiometric magnetite T_C, but also in samples FL and ETP where the same lower temperature T_C was already present, unlike in Jackson and Bowles' (2014) samples.

The clear absence of LT titanohematite features and the reproducibility of the high T_C temperatures suggest that the more stoichiometric magnetite contribution is primary, and the same is true for the lower temperature T_C, which can be attributed to high-titanium (∼50–60 per cent substitution) titanomagnetite in all samples. The Plinian tephra, as well as the recent ARJP products are thus dominated by high-Ti titanomagnetite and variable, but subordinate, amounts of more stoichiometric magnetite. In contrast, the Strombolian/sub-Plinian tephra are dominated by more stoichiometric magnetite and variable, yet subordinate, amounts of titanomagnetite. One exception is the sub-Plinian Bronte 1990 tephra, for which the M_s–T curves reveal striking similarities to the products of the most explosive Plinian and ARJP eruptions (Fig. S3). We speculate that such behaviour is due to the increased titanium content of this particular eruption, linked to recent changes in volcanic activity observed at Etna since 1990, as discussed in Section 5.4.2.

The presence of titanium obscures the Verwey transition (T_v), which can only be observed as a small 'bump' in the derivative of the FC and ZFC magnetization of the sub-Plinian FL, TV and Plinian (ET97-70/80-81cm) tephra, further confirming reduced titanium substitution for these samples (Fig. 8). Likewise, the more

pronounced, yet broad, decrease in RTSIRM for the same samples around the T_v (∼120 K) on cooling, is consistent with smaller titanium content compared to FG and Recent tephra, for which T_v is almost entirely suppressed (Fig. 8). Additionally, all samples reveal curvature of the RTSIRM curves upon cooling and warming, consistently with the 'humpiness' identified by Özdemir & Dunlop (2010) as the hallmark of maghemitization.

These observations, including the direct information obtained from Mössbauer spectroscopy (Fig. S1) and SEM analysis (Fig. S2), are fully compatible with petrological observations from low-silica alkaline melts, as those of Mt Etna, in which ilmenite crystallization is suppressed (e.g. Carmichael *et al.* 1974; Mollo *et al.* 2013). The magnetic signature observed here is attributed to dominant high undercooling and high decompression rates associated with explosive eruptive conditions, as discussed in Section 5.4.1.

5.2 Grain size and domain state

The ∼ parallel to pot-bellied hysteresis loops of the Plinian Late Pleistocene tephra and the Strombolian/sub-Plinian samples indicate a predominance of soft single coercivity contribution (Fig. 3). On the Day-Dunlop plot, the cluster of the strombolian/sub-plinian samples close to the SD-MD mixing lines suggests ∼50–70 per cent mixtures of the two components and also indicates minor grain size variations among these samples (Fig. 5). On the contrary, the Strombolian/sub-Plinian samples from the 1990 and 1998 eruptions are characterized by lower values of hysteresis parameters and notable constriction of the 1998 tephra loop (Table 1 and Fig. 5). Hysteresis parameters on a Day plot are ambiguous when characterizing complex mixtures that are typical of natural magnetic particle assemblages, making the interpretation of the domain state challenging (e.g. Roberts *et al*. 2018, 2019). The Néel plot is likely more indicative: overall, M_{rs}/M_s values vary between 0.05 and 0.3, and B_c data are confined between 3 and 25 mT (Fig. 5, Table 1), a range that would place all samples within the theoretical boundaries of the uniaxial single domain (USD) + superparamagnetic (SP) grains with axial ratios of 1.3:1 and 2:1, respectively (e.g. Tauxe *et al*. 2002), and modest to significant titanium substitution in all samples.

Magnetostatic interactions and internal stresses are additional factors controlling the domain state in titanomagnetites and are difficult to quantify (e.g. Roberts *et al.* 2018). However, internal stress may certainly affect tephra erupted under variable temperatures and pressures, and potentially results in the additional scatter observed in the Day plot for the Recent (2002, ARJP) daily ashes, on top of true grain size variations (Fig. 5a). The general position of the tachylite-rich (and tachylite extracts) and sideromelane fractions at the opposite ends of the Néel plot, and in particular with the tachylite at the high Bc end of the plot, and closer to the SD-SP mixing lines on the Day plot, do testify to the correlation between granulometry/coercivity and magma fragmentation.

Unmixing of the backfield remanence curves confirms that the Plinian eruptions from Unit D together with the sub-Plinian TV and FL tephra are dominated (86–89 per cent) by a component (∼36–49 mT), that can be considered SD, with a secondary soft (MD) component accounting for the remaining ∼11–14 per cent of the remanence (Fig. 10). Plinian FG and ARJP tephra exhibit a dominant component with values of ∼60–115 mT confirming that these tephra have overall higher coercivity as also indicated by the wasp-waisted hysteresis loops (Fig. 3). The presence of MD-PSD features as well as prominent higher coercivity distributions in the FORC diagrams strengthen these observations of contrasting coercivity distributions in these samples (Fig. 4).

Low temperature susceptibility data of all samples below ∼100 K possess a frequency dependent anomaly and peak in both the χ and χ', respectively. Such features have been widely reported for purely MD magnetite samples, increasing in magnitude with increasing grain size, and their origin resides in domain wall relaxation below the Verwey transition (Šimša *et al*. 1985; Skumryev *et al*. 1999; Kosterov 2003; Muxworthy 1999; Moskowitz *et al.* 1998; Church *et al.* 2011; Wang *et al*. 2021). Above 150 K, χ, peaking below room temperature for sample ET97-70/80-81 but increasing above 300 K for all other samples, represents the contribution of the finer SP and SD titanomagnetite fraction (e.g. Worm & Jackson, 1999; Till *et al.* 2011). In particular, χ' frequency-dependent peaks below room temperature isolate the SP contribution of these tephra (Worm & Jackson 1999; Till *et al.* 2011). Higher absolute susceptibility values for the Plinian FG and ARJP tephra, and better definition of the low and higher temperature χ' peaks, indicate higher concentrations of (Ti)magnetite in the different grain size fractions as well as greater fractionation for the respective eruptions.

Low temperature remanence curves, and specifically the R_{LT} ratio (Smirnov 2009) consistently around 1.1 (Table 1) calculated from the FC-ZFC curves, indicates that the remanence of the samples is carried by mixtures of SD and PSD-MD particles in all samples (Smirnov 2009). Moreover, the non-complete recovery of the RTSIRM curves upon temperature cycling through the anisotropic transition (130 K) and T_v, revealing ∼5–7 per cent loss for the FG and ARJP tephra, respectively, compared to ∼15–17 per cent loss in the Pleistocene Plinian eruptions and TV and FL Holocene sub-Plinian tephra, respectively, clearly indicates that the latter contain a relative higher proportion of MD grains compared to the finer fraction (Table 1).

All rock-magnetic evidence collected thus unequivocally supports the presence of a (Ti)magnetite mineralogy with some degree of oxidation for all samples. The FG and ARJP tephra are interpreted as being characterized by higher titanomagnetite content, higher abundance of magnetic minerals, particularly in the finer fraction (SP and SD), and higher fractionation, conferring higher coercivity to the samples.

The same magnetic features are not observed in the Pleistocene Plinian tephra, which, while similar to the FG and Recent tephra in terms of titanium substitution, show stronger affinity with the sub-Plinian TV and FL tephra in terms of coercivity/grain size and fractionation. The causes for such differences are discussed in Section 5.4.1.

5.3 Tachylite and sideromelane magnetic fingerprints

The tachylite and sideromelane fractions had been extracted from the two most fractionated products (Holocene FG Tephra and Recent ARJP 2002 eruption).

The M_{rs}/M_s and B_c and B_{cr}/B_c parameters place the two components, at around the opposite ends of the Day et al. and Néel plots, with the tachyle fractions defining an upper trend sub-parallel to the SD-SP mixing line and the sideromelane closer to the SD-MD mixing lines of the Day et al. plot, and both at the right and left (high and low coercivity end of the Néel plot. From these trends it is easily observed that the tachylite is generally characterized by smaller grain size owing to the generally larger M_{rs}/M_s ratio and higher coercivity, and with approximately two to five times larger magnetization (Fig. 10 and Table 1).

The coercivity difference is best-appreciated by the components isolated through unmixing of the remanence curves where the dominant peak is centred around ∼75–108 mT for the tachylite, as opposed to the ∼33–39 mT for the sideromelane, with the tachylite also possessing a softer, ∼25–30 mT component. Both fractions also possess an even lower, yet broader, minor coercivity component (Fig. 10). Such coercivity differences are interpreted to be responsible for the prominent wasp-waisted character of the tachylite hysteresis loops, as opposed to the generally narrower sideromelane loops. We iterate, however, that admixtures of SP grains, also present in the sideromelane fraction, and can result in constriction of the hysteresis loops (Tauxe *et al.* 1996; Roberts *et al.* 1995, Fig. 10 and Table 1). The tachylite fraction is also responsible for the observed higher coercivity distributions on the FORC diagrams (Fig. 10), all implying a negligible contribution of the hard fraction in the volcanic glass.

At low temperature, both fractions possess the low temperature (∼60–100 K) frequency-dependent χ anomalies and χ' peaks attributed to MD grains, with χ increasing above room temperature, and χ' peaking below room temperature, diagnostic of the SD-SP fraction, as observed in the bulk samples. Also consistently with the bulk samples, the absence of Verwey transition in all low temperature remanence curves reflects the increased Ti-substitution, and the greater SIRM loss at room temperature for the sideromelane (9.7 per cent) than for the tachylite (4.2 per cent) also confirms the increased MD contribution in the former (Fig. 10).

These observations suggest that the overall composition of the two components is similar, however, the higher room temperature magnetization and low temperature susceptibility of the tachylite implies increased magnetic particle concentration, and particularly of the SP fraction, corroborating the stronger coercivity contrast of the tachylite and tachylite-bearing samples as observed in the remanence unmixing curves, the more prominent wasp-waisted character of the hysteresis loops, also generally placing the tachylite samples closer to the SD-SP mixing lines of the Day plot (Fig. 5a) and at the higher Bc end of the Néel plot (Fig. 5b), as well as in the FORC distributions (Fig. 10).

5.4 Magnetic fingerprinting of the Mt Etna tephra and relationships with the eruptive styles

5.4.1 Composition and eruptive conditions

For explosively erupted and rapidly cooled materials, the Fe–Ti oxide compositions reflect the conditions in the magma storage region prior to eruption (Venezky & Rutherford 1999). Several studies on basaltic rocks have demonstrated, by means of chemical and magnetic measurements, that the Ti content in titanomagnetite is dependent on the kinetic conditions of the system (Smith & Prévot 1977; Zhou *et al.* 2000; Kissel *et al.* 2010; Mollo *et al.* 2011, 2012, 2013), however, its fundamental magnetic properties, in relationship with composition, form, temperature dependence and degree of cation ordering, are still not fully understood (e.g. Bowles *et al.* 2013, Jackson & Bowles 2018, and references therein). According to Zhou *et al.* (2000), titanomagnetite compositional variation depends on: (i) the temperature and local melt composition (including oxygen fugacity); (ii) metastable thermodynamic control and (iii) kinetic control. The role of both temperature and oxygen fugacity on titanomagnetite Ti-content was also recognized by Ghiorso & Sacks (1991), and thermodynamic calculations show that titanomagnetite content, $x(Fe_3\text{-}xTixO_4)$, in equilibrium with the melt and other minerals, decreases from 0.6 at 950 °C to 0.2 at 700 °C (Zhou *et al.* 2000). While redox conditions at Etna do not change after degassing, cooling and crystallization, Mollo *et al.* (2013) investigated the role of cooling rate on crystal morphology. Subeuhedral titanomagnetite crystals are formed at low cooling rates, but they are replaced by texturally immature dendrites if cooled more rapidly (Mollo *et al.* 2013). As cooling rate increases, diffusion cannot supply both Ti and Fe to the growing crystals at the equilibrium proportion, causing much lower Ti concentration in the melt adjacent to the crystal surface. Ovalle *et al.* (2018) observed that for explosive volcanism, systematic increases in magnetite titanium concentration are associated with volcanic systems transitioning from purely magmatic to magmatic-hydrothermal conditions.

Our data show that the amount of Ti varies among the three groups of ash samples, but variations are observed on different temporal scales. For example, in the Plinian samples from core ET97-70, the difference in susceptibility between 400 and 10 A m^{-1} fields shows a ∼25 per cent amplitude-dependent peak at the bottom of the core (Fig. 2), reflecting increased titanium content (e.g. Jackson *et al.* 1998) that is not as prominent in the upper portion. Therefore, the ash representative of the D1b-D2b eruptions are interpreted as being characterized by lower Ti content than the older D1a-D2a eruptions. The strong explosive activity responsible for the emplacement of Unit D was produced by the emptying of a large magma chamber with a more evolved benmoreitic/trachitic composition (Del Carlo *et al.* 2004) where the strong explosive activity is due to a volatile saturation in the magma chamber. Such emplacement mechanism is different from that of the basaltic Plinian FG eruption, which is instead attributed to rapid syn-eruptive crystallization leading to explosive fragmentation under high strain rates in open vent conditions (Arzilli et al. 2019). These distinctions are responsible for the different magnetic fingerprints observed among Plinian eruptions.

5.4.2 Fragmentation, eruptive style and nanolites

On a longer timescale, the identification of magnetic populations with contrasting grain sizes and coercivity distributions can be considered a discriminant factor among different styles of explosive activity. Higher coercivities and larger coercivity contrasts, indicative of large grain size variation, are clearly identified in samples representing more explosive eruptions dominated by the presence of tachylite (i.e. Holocene FG tephra, Recent ARJP eruptions), in good agreement with the ranges obtained from the tachylite fraction extracted from the same samples. In contrast, Strombolian/sub-Plinian tephra exhibit softer coercivity distributions, comparable to those observed in the sideromelane fraction (Fig. 9 and Table 1).

Importantly, differences exist between the magnetic properties of the recent (1990, 1998) sub-Plinian eruptions with respect to the Holocene sub-Plinian/strombolian tephra (TV, FL, FS and ETP), which could be an indication of the changing volcanic activity recognized at Etna during the last few decades: since 1990, Etna has produced an increasing number of violent explosive events characterized by the formation of plumes and including fire fountains that had never been observed before (Branca and Del Carlo, 2005). Furthermore geochemical variations in the geochemistry of erupted products since the 1971 eruption are considered as one of the most important recent petrological turning points in the evolution of the volcano (Viccaro & Cristofolini, 2008).

If a correlation exists between coercivity and explosivity, we speculate that the scattering of the samples representing the 2002

eruptions in the Day plot may represent different explosive styles alternating during the eruptions (Andronico *et al.* 2009). In this view, it is noteworthy that from unmixing of the backfield curves (Fig. 9), the highest coercivity is observed in the sample collected on the 30th of October, marking the beginning of the explosive activity. As suggested by Andronico *et al.* (2009), it is noteworthy that ARJP at Etna (2001–2002) do not occur under open vent conditions, but exclusively in correspondence of narrower and cooler flank eruptions that can favor a higher magma crystallization with respect to the larger and hotter central conduit.

The magnetic parameters reported here, and particularly the coercivity distributions, successfully discriminate among eruptive styles: the presence of tachylite over sideromelane appears to be the discriminant factor for explosive activity, and effectively characterizes the magnetic fingerprint of the corresponding tephra. Specific to the 2001 eruption ash, Taddeucci *et al.* (2004) numerically show that the oxide size distribution of the tachylite requires a longer and more complex history than the sideromelane, including two distinct nucleation events. These two distinct nucleation events likely represent the formation mechanism for the two magnetic populations with contrasting grain-sizes and coercivities, responsible for the wasp-waisted loops and the FORC distributions observed here.

Recently, few authors (Di Genova *et al.* 2020; Caceres *et al.* 2020, 2021) observed that a small volume of nano-sized crystals (nanolites) can be responsible for an increased magma viscosity. Colombier *et al.* (2017) identified Fe-Ti-oxide nanolites in tephra from Kilian volcano (France) that they consider as nuclei for heterogeneous nucleation of the very small vesicles. Furthermore Fe-Ti oxides are the main mineral phase that acts as an energetically favorable nucleation site for gas bubbles (Hurwitz & Navon 1994). By combining data, including from the FG tephra studied here, and numerical modeling, Di Genova *et al*. (2020) demonstrated that a few volume per cent of nanolites was responsible for a marked increase in viscosity above the critical value needed for explosive fragmentation during magma cooling and ascent. Raman spectra investigations (Di Genova *et al.* 2017, 2020) indicate that both quenching from above liquidus conditions and heating above the glass transition temperature, induced nanoscale crystallization of iron oxides, as further confirmed by *in situ* high-energy XRD experiments on molten Etna basalt, showing that unit cells of magnetite represent the first precipitating phases upon cooling. We speculate that the SP grain population of the tachylite samples represent the iron-bearing nanocrystals (nanolites) responsible for increased melt viscosity, leading to explosive activity, and are responsible for the magnetic signature of the more explosive eruptions generating the Plinian FG and Recent ARJP tephra.

5.4.3 Crystal texture and coercivity

According to Polacci *et al.* (2019), ash particle characteristics vary with eruptive style, and are responsible for peculiar textural and compositional features of ash particles at Etna. Ash emitted during Strombolian explosions and at the peak of lava fountain activity appears more vesicular and less crystallized, with a compositionally less evolved groundmass and less lithic material compared to ash erupted during less explosive events or at the end of a long-lasting explosive eruption. These differences invariably affect the magnetic properties and, although the observations by Polacci *et al.* (2019) were obtained from recent (post-1995) eruptions only, it is likely that they can be extended to longer timescales.

SEM observations of the bulk TV tephra (S26-TV) and of the tachylite fraction extracted from the FG tephra indicate that the former contain <5 μm euhedral titanomagnetite grains, whereas larger, <50 μm, grains with subskeletal texture characterize the tachylite (Fig. S2). The presence of skeletal crystals with irregular shapes affects the domain state of the samples: dendritic texture of titanomagnetite usually forms as the result of rapid cooling, while crystal composition, size, geometry and symmetry are controlled by cooling rate, oxygen fugacity, temperature gradient and impurities (Shaar & Feinberg 2013), likewise, the magnetization of Ti-rich titanomagnetites is controlled by stress-induced anisotropy (O'Reilly 1984; Özdemir & Moskowitz 1992) resulting from complex domain structures (Moskowitz *et al.* 1988). The rock-magnetic properties of grains with shape anisotropy can give rise to high coercivities, as observed in skeletal particles occurring in oceanic basalts by Kent & Gee (1996) and also determined from micromagnetic modeling of grains with complex shapes (Tauxe *et al.* 2002), providing a reasonable source for the high coercivity of the tachylite-bearing samples. Further evidence is provided by Mollo *et al.* (2015), who observe intricate intergrowth textures in titanomagnetites from lava fountains at Etna, interpreted to represent crystal attachment and agglomeration mechanisms.

6 CONCLUSIONS

A detailed rock magnetic study, including high/low temperature magnetization remanence and susceptibility experiments, hysteresis and FORC measurements, Mössbauer spectroscopy and SEM microscopy, was conducted on a collection of tephra samples erupted during the last 18 ka at Etna. Results suggest the presence of distinct magnetic signatures for ashes produced by different types of explosive activity.

The higher magma fragmentation that distinguishes the most explosive eruptions is responsible for the presence of tachylite for these products, which in turn are characterized by a distinctive magnetic fingerprint. Rock magnetism thus provides a useful tool to discriminate between explosive Plinian and ARJP styles of eruptions that generate tachylite from Strombolian/sub-Plinian eruptions for which sideromelane glass is more common. Additional variations in magnetic mineralogy and grain size are useful discriminants of the eruptive styles, and the following conclusions can be drawn based on the results of this study:

(i) High T experiments indicate that Strombolian/sub-Plinian FL, TV, ETP tephra contain a higher abundance of more stoichiometric magnetite, whereas titanomagnetite dominates the products of the more explosive Plinian and Recent Eruptions.

(ii) The magnetic mineralogy is characterized by variable contribution of MD and SP-SD grains, with a distinctly higher relative proportion of the latter in the highly explosive products. The contrasting grain size and coercivity distributions constitute a distinguishing magnetic signature of the tachylite fraction, representing a discriminant factor among explosive activity styles.

(iii) The magnetization of the Etna Ti-rich titanomagnetites is probably controlled by stress-induced anisotropy arising from the fractionation processes, and, together with the larger grain size distribution, is interpreted to contribute to the increased coercivity and wasp-waisted character of the hysteresis loops and coercivity populations observed in unmixing and FORC distributions of the most explosive products.

(iv) The SP grain population of the tachylite-rich samples, identified primarily through hysteresis measurements and LT experiments, may represent the iron-bearing nanocrystals (nanolites) considered to be responsible for increased melt viscosity, leading to explosive activity. This observation could thus support the interpretation that iron oxide nanolites may play a role in controlling the eruptive style, and, in turn, the petrological evolution of basaltic magmas.

(v) The distinct magnetic signature of the crystalline tachylite components of the juvenile clasts in the ash samples, as opposed to the glassy sideromelane, is therefore well-suited to distinguish the products of the explosive activity associated with certain Plinian eruptions and *ARJP* (FG and Recent 2002 tephra), noting, however, that not all Plinian products contain the tachylite and sideromelane fraction (e.g. the Late Pleistocene tephras). We also iterate that while the sideromelane fraction was also isolated from the most explosive FG and ARJP products, this component is more typical of Strombolian eruptions and should therefore not be used as a strict discriminant of eruptive style.

These preliminary observations indicate that rock magnetism may constitute a valuable tool for investigating the mechanisms of explosive basaltic eruptions, their eruptive styles and magma fragmentation, in relation to dynamic and kinetic conditions within the volcanic conduit. Magnetic parameters could prove helpful in monitoring ash features of early emitted tephra that are already used in forecasting impending eruptions (i.e. Watanabe *et al.* 1999). Additional studies on other volcanoes and different geodynamic contexts will establish trends indicative of the underlying eruptive styles and magmatic conditions.

ACKNOWLEDGMENTS

This work was partially supported by the Gruppo Nazionale per la Vulcanologia (GNV) Project 1999-2001 and by an IRM visiting Fellowship (LV)We thank Mauro Coltelli for the help in the field and C. Laj, C. Kissel, V. Scao for the use of the lab and measurements of thermomagnetic curves at CNRS in Gif sur Yvette. Peat Sølheid is thanked for acquiring the Mössbauer spectra and helping with the fits and interpretation. We thank Franco Corticelli (IMM-CNR) for help in SEM observations and photos. The Institute for Rock Magnetism is a U.S. National multi-user facility supported through the Instrumentation and Facilities program of the National Science Foundation, Earth Sciences Division and by funding from the University of Minnesota. This is IRM publication #2104

DATA AVAILABILITY

Data and metadata carried out at IRM and underlying this article are available at zenodo.org depository https://zenodo.org/record/6761888#.Yrwa1XZBxPZ; doi: 10.5281/zenodo.6761888.

CONFLICT OF INTEREST

The authors declare that no conflict of interest exists.

EFERENCES

Albert, P.G. *et al.*, 2013. Late glacial explosive activity on Mount Etna: implications for proximal-distal tephra correlations and the synchronisation of Mediterranean archives, *J. Volc. Geotherm. Res.,* **265,** 9–26.

Andronico, D. *et al.*, 2005. A multi-disciplinary study of the 2002–03 Etna eruption: insights for a complex plumbing system, *Bull. Volcanol.,* **67,** 314–330.

Andronico, D., Cannata, A., Di Grazia, G. & Ferrari, F., 2021. The 1986–2021 paroxysmal episodes at the summit craters of Mt. Etna: insights into volcano dynamics and hazard. *Earth-Sci. Rev.,* **220,** doi:10.1016/j.earscirev.2021.103686.

Andronico, D., Cristaldi, A., Del Carlo, P. & Taddeucci, J., 2009. Shifting styles of basaltic explosive activity during the 2002–03 eruption of Mt. Etna, Italy, *J. Volc. Geotherm. Res.,* **180,** 110–122.

Andronico, D., Scollo, S., Cristaldi, A. & Caruso, S., 2008. The 2002–03 Etna explosive activity: tephra dispersal and features of the deposit, *J. geophys. Res.,* **113**(B4), doi:10.1029/2007JB005126.

Arzilli, F. *et al.*, 2019. Magma fragmentation in highly explosive basaltic eruptions induced by rapid crystallization, *Nat. Geosci.,* **12,** 1023–1028.

Bowles, J. A., Jackson, M. J., Berquò, T. S., Solheid, P. A. & Gee, J. S., 2013. Inferred time- and temperature-dependent cation ordering in natural titanomagnetites. *Nat. Commun.,* **4,** doi:10.1038/ncomms2938.

Branca, S. & Del Carlo, P., 2005. Types of eruptions of Etna volcano AD 1670–2003: implications for short-term eruptive behavior, *Bull. Volcanol.,* **67**(8), 732–742.

Cáceres, F. *et al.*, 2020, Can nanolites enhance eruption explosivity?, *Geology,* **48**(10), 997–1001.

Cáceres, F., Scheu, B., Hess, K. U., Cimarelli, C., Vasseur, J., Kaliwoda, M. & Dingwell, D. B., 2021. From melt to crystals: the effects of cooling on FeTi oxide nanolites crystallisation and melt polymerisation at oxidising conditions, *Chem. Geol.,* **563,** doi:10.1016/j.chemgeo.2021.120057.

Calanchi, N., Dinelli, E., Gasparotto, G. & Lucchini, F., 1996. Etnean tephra layer in Albano Lake and Adriatic Sea cores: new findings Y-1 layer in Central Mediterranean area, *Acta Vulcanol.,* **8,** 7–13.

Cannata, C. B., De Rosa, R., Donato, P. & Taddeucci, J., 2014. Ash features from ordinary activity at Stromboli Volcano, *Int. J. Geosci.,* **05,** 1361–1382.

Carmichael, I.S.E., Turner, F.J. & Verhoogen, J., 1974. *Igneous Petrology*. McGraw–Hill. 739pp.

Carter-Stiglitz, B., Banerjee, S.K., Gourlan, A. & Oches, E., 2006. A multi-proxy study of Argentina loess: marine oxygen isotope stage 4 and 5 environmental record from pedogenic hematite, *Palaeogeogr. Palaeoclimatol. Palaeoecol.,* **239,** 45–62..

Cashman, K. & Blundy, J., 2000. Degassing and crystallization of ascending andesite and dacite, *Phil. Trans. R. Soc. Lond., A,* **358,** 1487–1513.

Cassidy, M., Manga, M., Cashman, K. & Bachmann, O., 2018. Controls on explosive-effusive volcanic eruption styles, *Nat. Comm.,* **9,** 2839.

Church, N., Feinberg, J. M. & Harrison, R., 2011. Low-temperature domain wall pinning in titanomagnetite: quantitative modeling of multidomain first-order reversal curve diagrams and AC susceptibility, *Geochem. Geophys. Geosyst.,* **12**(7), doi:10.1029/2011GC003538.

Colombier, M., Gurioli, L., Druitt, T.H., Shea, T., Boivin, P., Miallier, D. & Cluzel, N., 2017. Textural evolution of magma during the 9.4-ka trachytic explosive eruption at Kilian Volcano, Chaîne des Puys, France, *Bull. Volcanol.,* **79,** 17.

Coltelli, M., Del Carlo, P., Pompilio, M. & Vezzoli, L., 2005. Explosive eruption of a picrite: the BP sub-Plinian eruption of Etna volcano (Italy), *Geophys. Res. Lett.,* **32**(23), 4.

Coltelli, M., Del Carlo, P. & Vezzoli, L. 1998. Discovery of a Plinian basaltic eruption of Roman age at Etna volcano, Italy, *Geology,* **26**(12), 1095–1098.

Coltelli, M., Del Carlo, P. & Vezzoli, L., 2000. Stratigraphic constraints for explosive activity in the last 100 ka at Etna volcano, *Italy, Int. J. Earth Sci.,* **89,** 665–677.

Day, R., Fuller, M.D. & Schmidt, V.A., 1977. Hysteresis properties of titanomagnetites: grain-size and compositional dependence, *Phys. Earth planet. Inter.,* **13,** 260–267.

De Rita, D., Frazzetta, G. & Romano, R., 1991. The Biancavilla-Montalto ignimbrite (Etna, Sicily), *Bull. Volcanol.,* **53,** 121–131.

Del Carlo, P., Branca, S. & D'Oriano, C., 2017. New findings of Late Glacial Etna pumice fall deposits in NE Sicily and implications for distal

tephra correlations in the Mediterranean area, *Bull. Volcanol.,* **79**(50), doi:10.1007/s00445-017-1135-7.

Del Carlo, P., Vezzoli, L. & Coltelli, M., 2004. Last 100 ka tephrostratigraphic record of Mount Etna, in *Mt Etna: Volcano Laboratory, Geophysical Monograph Series,* Vol. **143,** pp. 77–89, eds Bonaccorso, Alessandro, Calvari, Sonia, Coltelli, M., Del Negro, C. & Falsaperla, S., AGU.

Di Genova, D. *et al.*, 2020. In situ observation of nanolite growth in volcanic melt: a driving force for explosive eruptions, *Sci. Adv.,* **6**(39), doi:10.1126/sciadv.abb0413.

Di Genova, D., Kolzenburg, S., Wiesmaier, S., Dallanave, E., Neuville, D., Hess, K.U. & Dingwell, D.B., 2017. A chemical tipping point governing mobilization and eruption style of rhyolitic magma, *Nature,* **552,** 235–238.

Dingwell, D.B., 1996. Volcanic dilemma: flow or blow? *Science,* **273**(5278), 1054–1055.

Dunlop, D.J., 2002. Theory and application of the Day plot (Mrs/Ms versus Hcr/Hc) 1. Theoretical curves and tests using titanomagnetite data, *J. geophys. Res.,* **107,** doi:10.1029/2001JB000486.

Dunlop, D.J. & Özdemir, Ö., 1997. *Rock Magnetism: Fundamentals and Frontiers,* Cambridge Univ. Press. 573pp.

Egli, R. 2021. Magnetic characterization of geologic materials with first-order reversal-curves, in *Magnetic Measurement Techniques for Materials Characterization,* eds Franco, V. & Dodrill, B., Springer International Publishing Group, 815pp.

Egli, R. 2013.VARIFORC: an optimized protocol for calculating non-regular first-order reversal curve (FORC) diagrams, *Glob. Planet. Chang.* **110,**302–320.

Fabian, K., 2003. Some additional parameters to estimate domain state from isothermal magnetization measurements, *Earth planet. Sci. Lett.,* **213**(3), 337–345.

Ghiorso, M.S. & Sack, R.O., 1991. Fe-Ti oxide geothermometry: thermodynamic formulation and the estimation of intensive variables in silicic magmas, *Contrib. Mineral. Petrol.,* **108,** 485–510.

Giordano, D. & Dingwell, D.B., 2003. Viscosity of hydrous Etna basalt: implications for Plinian-style basaltic eruptions, *Bull. Volcanol.,* **65,** 8–14.

Gonnermann, H.M., 2015. Magma fragmentation, *Annu. Rev. Earth planet. Sci.,* **43**(1), 431–458.

Gonnermann, H.M. & Manga, M., 2003. Explosive volcanism may not be an inevitable consequence of magma fragmentation, *Nature,* **426,** 432–435.

Harrison, R.J. & Feinberg, J.M., 2008. FORCinel: an improved algorithm for calculating first order reversal curve distributions using locally weighted regression smoothing, *Geochem. Geophys. Geosyst.,* **9**(5), doi:10.1029/2008GC001987.

Head, J.W. & Wilson, L., 1989. Basaltic pyroclastic eruptions: influence of gas-release patterns and volume fluxes on fountain structure, and the formation of cinder cones, spatter cones, rootless flows, lava ponds and lava flows, *J. Volc. Geotherm. Res.,* **37,** 261–271.

Heiken, G. & Wohletz, K.H., 1985. *Volcanic Ash*. Univ. California Press, 246pp.

Hurwitz, S. & Navon, O., 1994. Bubble nucleation in rhyolitic melts: experiments at high pressure, temperature, and water content. *Earth planet Sci. Lett.* **122,** 267–280.

Jackson, M. & Bowles, J.A., 2014. Curie temperatures of titanomagnetite in ignimbrites: effects of emplacement temperatures, cooling rates, exsolution, and cation ordering, *Geochem. Geophys. Geosyst.,* **15,** 4343–4368.

Jackson, M., Moskowitz, B., Rosenbaum, J. & Kissel, C. 1998. Field-dependence of AC susceptibility in titanomagnetites, *Earth planet. Sci. Lett.,* **157**(3–4), 129–139.

Jackson, M.J. & Bowles, J.A., 2018. Malleable Curie temperatures of natural titanomagnetites: Occurrences, modes, and mechanisms, *J. geophys. Res.,* **123,** 921–940.

Kasama, T., Harrison, R.J., Church, N.S., Nagao, M., Feinberg, J.M. & Dunin-Borkowski, R.E. 2013. Ferrimagnetic/ferroelastic domain interactions in magnetite below the Verwey transition. Part I: electron holography and Lorentz microscopy, *Phase Transit*., **86**(1), 67–87.

Kent, D.V. & Gee, J. 1996. Magnetic alteration of zero-age oceanic basalt, *Geology,* **24,** 703–706.

Kissel, C., Laj, C., Sigurdsson, H. & Guillou, H., 2010. Emplacement of magma in Eastern Iceland dikes: insights from magnetic fabric and rock magnetic analyses. *J. Volc. Geotherm. Res.,* **191,** 79–92.

Knafelc, J. *et al.*, 2022. Havre 2012 pink pumice is evidence of a shortlived, deep-sea, magnetite nanolite-driven explosive eruption, *Commun. Earth Environ.,* **3,** 19.

Knott, T.R., Branney, M.J., Reichow, M.K., Finn, D.R., Tapster, S. & Coe, R.S., 2020. Discovery of two new super-eruptions from the Yellowstone hotspot track (USA): is the yellowstone hotspot waning?, *Geology,* **48**(9), 934–938.

Kosterov, A., 2003. Low-temperature magnetization and AC susceptibility of magnetite: effect of thermomagnetic history, *Geophys. J. Int.,* **154,** 58–71.

Kosterov, A. & Fabian, K., 2008. Twinning control of magnetic properties of multidomain magnetite below the Verwey transition revealed by measurements on individual particles, *Geophys. J. Int.,* **174**(1), 93–106.

La Spina, G., Burton, M. & de' Michieli Vitturi, M., 2015. Temperature evolution during magma ascent in basaltic effusive eruptions: a numerical application to Stromboli volcano, *Earth planet. Sci. Lett.,* **426,** 89–100.

Lagroix, F., Banerjee, S.K. & Jackson, M.J., 2004. Magnetic properties of the Old Crow tephra: identification of a complex iron titanium oxide mineralogy, *J. geophys. Res.,* **109**(B1), doi:10.1029/2003JB002678.

Lied, P., Kontny, A., Nowaczyk, N., Mrlina, J. & Kämpf, H., 2020. Cooling rates of pyroclastic deposits inferred from mineral magnetic investigations: a case study from the Pleistocene Mýtina Maar (Czech Republic), *Int. J. Earth Sci. (Geol Rundsch),* **109,** 1707–1725.

Maenaka, K. & Yokoyama, T., 1972. Ferromagnetic minerals involved in volcanic ash-layers of Osaka Group, Typical Plio-Pleistocene sediments in south-west Japan, *Quater. Res.,* **11,** 270–280.

Makaroğlu, Ö., Çağatay, M.N., Nowaczyk, N.R., Pesonen, L.J. & Orbay, N., 2018. Discrimination of Holocene tephra units in Lake Van using mineral magnetic analysis, *Quater. Int.,* **486,** 44–56.

Maxbauer, D.P., Feinberg, J.M. & Fox, D.l., 2016. MAX UnMix: A web application for unmixing magnetic coercivity distributions, *Comput. Geosci.,* **95,** 140–145

Mollo, S., Giacomoni, P.P., Andronico, D. & Scarlato, P., 2015. Clinopyroxene and titanomagnetite cation redistributions at Mt. Etna volcano (Sicily, Italy): footprints of the final solidification history of lava fountains and lava flows, *Chem. Geol.,* **406,** 45–54.

Mollo, S., Lanzafame, G., Masotta, M., Iezzi, G., Ferlito, C. & Scarlato, P., 2011. Cooling history of a dike as revealed by mineral chemistry: a case study from Mt. Etna volcano, *Chem. Geol.,* **288,** 39–52.

Mollo, S., Misiti, V., Scarlato, P. & Soligo, M., 2012. The role of cooling rate in the origin of high temperature phases at the chilled margin of magmatic intrusions, *Chem. Geol.,* **322-323,** 28–46.

Mollo, S., Putirka, K., Iezzi, G. & Scarlato, P. 2013. The control of cooling rate on titanomagnetite composition: implications for a geospeedometry model applicable to alkaline rocks from Mt. Etna volcano, *Contrib. Miner. Petrol.,* **165,** 457–475.

Moskowitz, B., Jackson, M. & Kissel, C., 1998. Low-temperature magnetic behaviour of Titanomagnetites, *Earth Planet. Sci. Lett.,* **157,** 141–149.

Moskowitz, B.M., Halgedahl, S.L. & Lawson, C.A., 1988. Magnetic domains on unpolished and polished surfaces of titanium-rich titanomagnetite, *J. geophys. Res.,* **93,** 3372–3386.

Muxworthy, A., 1999. Low-temperature susceptibility and hysteresis of magnetite, *Earth planet. Sci. Lett.,* **169,** 51–58.

Naumov, A.N., Burnatny, S.S., Minyuk, P.S. & Zubov, A.G., 2019. Rock magnetic properties of Pleistocene Tephras from the Polovinka section of the Central Kamchatka depression, in *Recent Advances in Rock Magnetism, Environmental Magnetism and Paleomagnetism,* pp. 273–295, eds Nurgaliev, D., Shcherbakov, V., Kosterov, A. & Spassov, S., Springer Geophysics.

O' Reilly, W., 1984. *Rock and Mineral Magnetism,* Chapman and Hall, 220pp.

Ovalle, J.T. *et al.*, 2018. Formation of massive iron deposits linked to explosive volcanic eruptions. *Sci. Rep.,* **8,** 14855.

Özdemir, Ö. & Dunlop, D.J., 2010. Hallmarks of maghemitization in low-temperature remanence cycling of partially oxidized magnetite nanoparticles, *J. geophys. Res.,* **115**(B2), doi:10.1029/2009JB006756.

Özdemir, Ö. & Moskowitz, B.M. 1992. Magnetostriction in aluminum-substituted titanomagnetites, *Geophys. Res. Lett.,* **19,** 2361–2364.

Polacci, M., Andronico, D., De Michieli, V.T., Taddeucci, J. & Cristaldi, A. 2019. Mechanisms of ash generation at basaltic volcanoes: the case of Mount Etna, Italy, *Front. Earth Sci.,* **7,** 193.

Risica, G., Di Roberto, A., Speranza, F., Del Carlo, P., Pompilio, M., Meletlidis, S. & Rosi, M., 2020. Refining the Holocene eruptive activity at Tenerife (Canary Islands): the contribution of palaeomagnetism, *J. Volc. Geotherm. Res.,*106930, **401,** doi:10.1016/j.jvolgeores.2020.106930.

Roberts, A.P. *et al.*, 2019. Domain state diagnosis in rock magnetism: evaluation of potential alternatives to the Day diagram, *J. geophys. Res.,* **124**(6), 5286–5314.

Roberts, A.P., Tauxe, L., Heslop, D., Zhao, X. & Jiang, Z., 2018. A critical appraisal of the 'Day' diagram, *J. geophys. Res.,* **123,** 2618–2644.

Roberts, A.P.,Cui, Y.L.& Verosub, K.L.,1995. Wasp-waisted hysteresis loops: Mineral magnetic characteristics and discrimination of components in mixed magnetic systems. *J. Geophys. Res.,* **100**(B9), 17909–17924.

Rosenbaum, J.G., 1986. Paleomagnetic directional dispersion produced by plastic deformation in a thick Miocene welded tuff, southern Nevada: implications for welding temperatures, *J. geophys. Res.,* **91,** 12 817–12 834.

Schlinger, C.M., Rosenbaum, J.G. & Veblen, D.R., 1988. Fe-oxide microcrystals in welded tuff from southern Nevada: origin of remanence carriers by precipitation in volcanic glass, *Geology,* **16,** 556–559.

Schlinger, C.M., Veblen, D.R. & Rosenbaum, J.G., 1991. Magnetism and magnetic mineralogy of ash flow tuffs from Yucca Mountain, Nevada, *J. geophys. Res.,* **96,** 6035–6052.

Scollo, S., Coltelli, M., Bonadonna, C. & Del Carlo, P., 2013. Tephra hazard assessment at Mt. Etna (Italy), *Nat. Haz. Earth Sys. Sci.,* **13**(12), 3221–3233.

Scollo, S., Del Carlo, P. & Coltelli, M., 2007. Tephra fallout of 2001 Etna flank eruption: analysis of the deposit and plume dispersion, *J. Volc. Geotherm. Res.,* **160,** 147–164.

Shaar, R. & Feinberg, J. M., 2013. Rock magnetic properties of dendrites: insights from MFM imaging and implications for paleomagnetic studies, *Geochem. Geophys. Geosyst.,* **14,** 407–421.

Šimša, Z., Y. Kawai, Y. & Beabers, V.A.M., 1985. Anelasticity and relaxation effects in single crystal Mn ferrites, *Phys. Stat. Solidi (a),* **88**(2), 611–617.

Skumryev, V., Blythe, H.J., Cullen, J. & Coey, J.M.D., 1999. AC susceptibility of a magnetite crystal, *J. Magn. Magn. Mater.,* **196-197,** 515–517.

Smirnov, A.V., 2009. Grain size dependence of low-temperature remanent magnetization I natural and synthetic magnetite: experimental study, *Earth Planets Space,* **61,** 119–124.

Smith, B.M. & Prevot, M., 1977. Variation of the magnetic properties in a basaltic dyke with concentric cooling zones, *Phys. Earth planet. Inter.* **14**(2), 120–136.

Smith, V.C., Isaia, R. & Pearce, N.J.G., 2011. Tephrostratigraphy and glass compositions of post-15 kyr Campi Flegrei eruptions: implications for eruption history and chronostratigraphic markers, *Quater. Sci. Rev.,* **30,** 3638–3660.

Sparks, R.S.J., Tait, S.R. & Yanev, Y., 1999. Dense welding caused by volatile resorption, *J. Geol. Soc.,* **156,** 217–225.

Taddeucci, J., Pompilio, M. & Scarlato, P., 2002. Monitoring the explosive activity of the July–August 2001 eruption of Mt. Etna (Italy) by ash characterization, *Geophys. Res. Lett.,* **29,** 71–1-71-4.

Taddeucci, J., Pompilio, M. & Scarlato, P., 2004. Conduit processes during the July–August 2001 explosive activity of Mt. Etna (Italy): inferences from glass chemistry and crystal size distribution of ash particles, *J. Volc. Geotherm. Res.,* **137,** 33–54.

Tanguy, J.C., Condomines, M., Branca, S., La Delfa, S. & Coltelli, M., 2012. New archeomagnetic and 226Ra-230Th dating of recent lavas for the Geological map of Etna volcano, *Ital. J. Geosci. (Boll. Soc. Geol. It.),* **131**(2), 241–257.

Tauxe, L., Bertram, H.N. & Seberino, C., 2002. Physical interpretation of hysteresis loops: micromagnetic modeling of fine particle magnetite, *Geochem. Geophys. Geosyst.,* **3**(10), doi:10.1029/2001GC000241.

Tauxe, L., Mullender, T.A.T. & Pick, T., 1996. Pot-bellies, wasp-waists and superparamagnetism in magnetic hysteresis, *J. geophys. Res.,* **101,** 571–583, 1996.

Till, J.L., Jackson, M.J., Rosenbaum, J.G. & Solheid, P., 2011. Magnetic properties in an ash flow tuff with continuous grain size variation: a natural reference for magnetic particle granulometry, *Geochem. Geophys. Geosyst.,* **12,** doi:10.1029/2011GC003648.

Venezky, D.Y. & Rutherford, M.J., 1999. Petrology and Fe–Ti oxide reequilibration of the 1991 Mount Unzen mixed magma, *J. Volc. Geotherm. Res.,* **89,** 213–230.

Viccaro, M. & Cristofolini, R., 2008. Nature of mantle heterogeneity and its role in the short-term geochemical and volcanological evolution of Mt. Etna (Italy), *Lithos,* **105**(3–4), 272–288.

Vigliotti, L., 2015. Magnetic properties of the Campanian Ignimbrite and the marine Y5 tephra layer, in *The Use of Palaeomagnetism and Rock Magnetism to Understand Volcanic Processes,* Vol. **396,** pp. 227–238, eds Ort, M.H., Porreca, M. & Geissman, J.W., Geological Society, London, Special Publications.

Vigliotti, L., Asioli, A., Bergami, C., Capotondi, L. & Piva, A., 2011. Magnetic properties of the youngest sapropel S1 in the Ionian and Adriatic Sea: inference for the timing and mechanism of sapropel formation, *Ital. J. Geosci. (Boll. Soc. Geol. It.),* **130**(1), 106–118.

Wang, S., Chang, L., Tao, C., Bilardello, D., Liu, L. & Wu, T., 2021. Seafloor magnetism under hydrothermal alteration: insights from magnetomineralogy and magnetic properties of the Southwest Indian Ridge basalts, *J. geophys. Res.,* **126,** e2021JB022646.

Watanabe, K., Danhara, T., Watanabe, K., Terai, K. & Yamashita, T., 1999. Juvenile volcanic glass erupted before the appearance of 1991 lava dome, Unzen Volcano, Kyushu, Japan, *J. Volc. Geotherm. Res.,* **89,** 113–121.

Westgate, J.A. *et al.*, 2018. Quaternary tephra from the Valles caldera in the volcanic field of the Jemez Mountains of New Mexico identified in western Canada, *Quart. Res.,* **91**(2), 813–828

Williams-Jones, G., Barendregt, R. W., Russell, J. K., Le Moigne, Y., Enkin, R. J. & Gallo, R., 2020. The age of the Tseax volcanic eruption, British Columbia, Canada, *Can. J. Earth Sci.,* **57**(10), 1238–1253.

Worm, H.-U. & Jackson, M. J., 1999. The superparamagnetism of Yucca Mountain Tuff, *J. geophys. Res.,* **104**(B11), 25 415–25 425,

Zhou, W., Van der Voo, R., Peacor, D.R. & Zhang, Y., 2000. Variable Ti-content and grain size of titanomagnetite as a function of cooling rate in very young MORB, *Earth planet. Sci. Lett.,* **179,** 9–20.

SUPPORTING INFORMATION

Supplementary data are available at *GJI* online.

Figure S1. Mossbauer results from the Plinian sample ET97-70/80-81, the sub-Plinian TV and the Recent ARJP (1/11/02). The Plinian and recent tephra were measured at low (18–20 K) whereas only the latter experiment was carried out for the holocenic tephra TV.

Figure S2. Scanning Electron Microscope (SEM) and mineralogical characterization of samples from the TV tephra (a) and tachylite from the FG tephra (b). Mineralogical characterization was made on the basis of punctual ESEM-EDS analysis of grains of titanomagnetite imaged by using back-scattered electrons at 20 kV in order to image the Fe and Ti.

Figure S3. Thermomagnetic experiments (Ms – °C) for selected Etna tephra: Plinian FG, ARJP and Strombolian/sub-Plinian samples. ARJP from 30/10/2002 was reheated and it shows full reversibility after the second heating.

Figure S4. Direct current (dc) magnetic remanence experiments for tephra samples from Plinian eruptions (a–b), ARJP (c–d) Strombolian/sub-Plinian eruptions (e–f) and sideromelane and tachylite samples (g–h). The measurements were carried out by

measuring the magnetic remanence on warming from 10 K to room temperature (300 K) after cooling in a 2.5 T saturation isothermal remanent magnetization (SIRM, field cooled remanence, FC, blue), as well as after cooling in zero field (ZFC, red) and applying a low temperature 2.5 T SIRM). Left axes for FC and FCZ measurements (open symbols); right axes for RTSIRM experiments (close symbols).

Table S1. Tabulated Mossbauer magnetic hyperfine parameters for the Plinian sample ET97-70/80-81, sub-Plinian sample S26-TV, and the Recent ARJP sample 1-11-2002, for the titanomagnetite cation tetrahedral site A and octahedral site B sextets, collected at 18–20 K and 295 K. BHF, maximum hyperfine field; QS, quadrupole splitting; IS, isomer shift.